Remote Sensing of Environment 318 (2025) 114597



Contents lists available at ScienceDirect

Remote Sensing of Environment

journal homepage: www.elsevier.com/locate/rse



Measuring river slope using spaceborne GNSS reflectometry: Methodology and first performance assessment

Yang Wang [a,*], Y. Jade Morton [a], J. Toby Minear [b], Alexa Putnam [a], Alex Conrad [c], Penina Axelrad [a], R. Steven Nerem [a], April Warnock [d], Christopher Ruf [e], Daniel Medeiros Moreira [f,g], Matthieu Talpe [h]

[a] Ann and H.J. Smead Aerospace Engineering Sciences Department, University of Colorado Boulder, Boulder, CO, USA
[b] Cooperative Institute for Research in Environmental Sciences, University of Colorado Boulder, Boulder, CO, USA
[c] Jet Propulsion Laboratory, California Institute of Technology, Pasadena, CA, USA
[d] SRI International, Ann Arbor, MI, USA
[e] Department of Climate and Space Sciences and Engineering, University of Michigan, Ann Arbor, MI, USA
[f] Department of Hydrology, Companhia de Pesquisa de Recursos Minerais, Geological Survey of Brazil, Rio de Janeiro, Brazil
[g] Géosciences Environnement Toulouse (GET), CNRS/CNES/IRD/UPS, Toulouse, France
[h] Spire Global, Luxembourg

ARTICLE INFO

Edited by Menghua Wang

Dataset link: https://podaac.jpl.nasa.gov/dataset/CYGNSS_L1_RAW_IF, https://www.earthdata.nasa.gov/esds/csda/smallsat-data-explorer, https://podaac.jpl.nasa.gov/SWOT, https://explore.creodias.eu/, VMF Data Server, http://cedar.openmadrigal.org, https://waterdata.usgs.gov/nwis, https://www.snirh.gov.br/hidroweb/serieshistoricas, https://www.theia-land.fr/en/hydroweb, https://www.theia-land.fr/en/typeofproduct/hydroweb-nexten/

Keywords:
GNSS reflectometry (GNSS-R)
Phase altimetry
Water surface height
River slope
Inland water
Lake
Geoid
Satellite altimetry
CYGNSS
Spire
SWOT

ABSTRACT

River slope, a crucial parameter in hydrological modeling, has historically been difficult to measure continuously on a regional or global scale. Satellite altimetry missions often have long revisit times, such as 10 to 20 days for the Surface Water and Ocean Topography (SWOT) mission. In this paper, a novel approach is presented utilizing spaceborne GNSS Reflectometry (GNSS-R) to measure river slopes with high accuracy and potentially short revisit times. Our Earth is enveloped in radio signals from over 100 GNSS satellites. These signals can be coherently reflected from river surfaces and detected by low Earth orbit (LEO) satellites with sufficient energy to estimate carrier phase. The carrier phase measurement captures water surface height variations, which can be extracted through modeling of the reflection signal propagation geometry and space environment effects to estimate river slopes. This study processes both the raw intermediate frequency (IF) data obtained by NASA's Cyclone GNSS (CYGNSS) microsatellites and the grazing-angle GNSS-R data generated by Spire Global nanosatellites to demonstrate the feasibility and performance of the GNSS-R based river slope retrieval. This paper focuses on selected river sections with width greater than ~500 meters. Detailed methodologies and error analyses are presented, indicating total uncertainty of approximately 0.38 cm/km plus ionospheric TEC model error for CYGNSS and 0.69 cm/km for Spire (with dual-frequency ionospheric correction) over an ideal 5-km river section at 30° elevation angle. The retrieval results are validated in areas with nearby flat water surfaces (such as lakes or wide and slow river sections) and against in situ gauge measurements and satellite altimetry, consistently demonstrating the high accuracy and reliability of spaceborne GNSS-R for measuring river slopes.

1. Introduction

River slope is a crucial parameter in hydrological modeling for estimating flow velocity and discharge. As illustrated in Fig. 1, river slope is the gradient of river water surface elevation (WSE) with respect to the geoid. It is typically determined using WSE measurements between an upstream and a downstream point or continuously along the stream (Alsdorf et al., 2007). For most rivers, their surface slopes are not stationary but can change over short time and length scales throughout the river course due to changes in upstream discharge, tributary inflow, flood waves associated with high precipitation, rapid

* Corresponding author.
E-mail address: yang.wang-2@colorado.edu (Y. Wang).

https://doi.org/10.1016/j.rse.2025.114597
Received 30 August 2024; Received in revised form 1 January 2025; Accepted 2 January 2025
Available online 22 January 2025
0034-4257/© 2025 The Authors. Published by Elsevier Inc. This is an open access article under the CC BY-NC-ND license (http://creativecommons.org/licenses/by-nc-nd/4.0/).

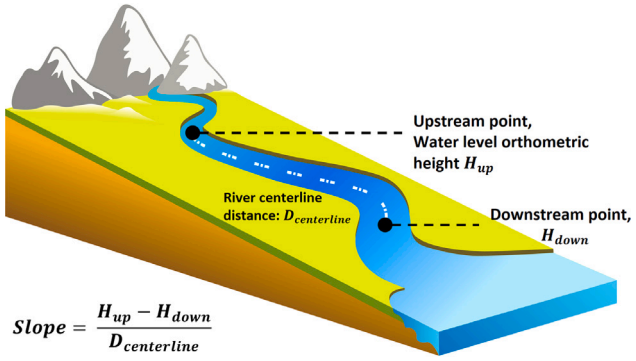


Fig. 1. Illustration of river slope.

mountain snow and glacier melt events due to warming, and riverbed deposition or erosion (Julien, 2018). River slopes can vary significantly over periods ranging from weeks, days to even hours, particularly during flooding events. The river slope values in hydrologic models, for example, the National Water Model (NWM), are often derived from topographic elevation models, which have significant errors and have been shown to impose substantial limitations on the model's performance (Heldmyer et al., 2021). Therefore, obtaining accurate and high temporal revisit river slope measurements is essential for improved modeling of river dynamics, optimal management of water resources, and prediction of future conditions including flood and drought hazards. Given that flooding is a major natural hazard globally, causing over $40 billion in damages annually and affecting more than 250 million people each year (OECD, 2016), precise and continuous monitoring of river slopes with GNSS-R could have significant societal impacts.

Measuring river slopes on regional or global scales has been challenging with conventional methods. While water level differences between two gauges can provide estimates of average river slopes between the gauges, the spatial distribution of these gauges is often sparse and they are typically separated by long distances, such as tens to hundreds of kilometers. As a result, the estimated average slopes over these long distances do not accurately represent all points along rivers and can be highly inaccurate for many locations. Moreover, the distribution of gauges is uneven, concentrated in developed countries and absent in remote areas such as the high-latitude Pan-Arctic basins to the equatorial Amazon and Congo basins. Many international regions also have restrictions on data sharing (Hannah et al., 2011). Smaller-scale local river slope variations can be measured by airborne lidar and radar and field measurements, but such campaigns require substantial and expensive efforts and thus are not suitable for continuous or large-scale observation. Global or large-scale monitoring of river surface elevations and gradients can be conducted from space using satellites.

Classical radar altimeters, such as the TOPEX/Jason series, operate in low-resolution mode and have decimeter-level errors in river water surface height measurements (Zakharova et al., 2020). Moreover, such single-beam satellite altimeters have inhomogeneous distribution of virtual stations along the river and lack simultaneous measurements. Sentinel 3A/B and Cryosat-2 can operate their synthetic aperture radars (SAR) in a fine-resolution mode (~300 m footprint) and measure inland water level with an accuracy and precision of a few to over ten centimeters (Schneider et al., 2017; Kleinherenbrink et al., 2020). The Ice, Cloud, and land Elevation Satellite-2 (ICESat-2), with its approximately 11-m footprint and simultaneous altimetry measurements from six laser beams, has been explored for measuring inland water levels, achieving an accuracy and precision at the centimeter level (Jasinski et al., 2021). Scherer et al. (2022) investigated using the ICESat-2 lidar measurements to derive river slopes and achieved a median absolute error of 2.3 cm/km for a global reach-scale water surface slope dataset. However, the incapacity of spaceborne lidar systems, such as ICESat-2, to operate in cloud-covered areas restricts their ability to provide observations during flooding or periods of heavy precipitation. The recently launched Surface Water and Ocean Topography (SWOT) mission, carrying the Ka-band Radar Interferometer (KaRIn), achieves a spatial resolution of approximately 50 to 100 m and a wide swath of ~120 km on each side of its ground track. SWOT has an expected accuracy of 1.7 cm/km for river slope measurement based on a 10-km downstream averaging of a 100-m wide ideal river (Esteban Fernandez et al., 2017), and enhanced accuracy is anticipated for wider rivers.

Satellite altimeters mentioned above all have relatively long revisit times (e.g., 10–20 days for SWOT in mid-latitudes and 91 days for ICESat-2), which highlights a significant knowledge gap in high-temporal (daily or sub-daily) surface water observation. This paper aims to demonstrate that accurate and precise river slope observations can be achieved by global navigation satellite systems reflectometry (GNSS-R) on small satellites for river sections wider than approximately 500 m. The relatively low cost, small size, and low power consumption of GNSS-R systems makes it practical to deploy a large constellation of small satellites to enable global and high temporal-resolution observations of river slopes.

Spaceborne GNSS-R is a passive remote sensing technique that leverages opportunistic L-band GNSS signals reflected off the Earth's surface. These reflections, which can be either diffusive or coherent, have been utilized in various remote sensing applications. Notable uses include ocean scatterometry and wind speed retrieval (Martin-Neira, 1998; Komjathy et al., 2000; Garrison et al., 2002; Zavorotny et al., 2004; Foti et al., 2015; Ruf et al., 2018; Liu et al., 2019), mapping the L-band Earth surface reflectivity and soil moisture (Katzberg et al., 2006; Rodriguez-Alvarez et al., 2009; Zavorotny et al., 2009; Chew and Small, 2018; Al-Khaldi et al., 2019), inland water/flooding inundation extent (Zuffada et al., 2016; Chew et al., 2016; Morris et al., 2019; Loria et al., 2020; Al-Khaldi et al., 2021; Pu et al., 2024; Zhang et al., 2022), freeze/thaw conditions (Wu et al., 2020; Carreno-Luengo and Ruf, 2021; Rautiainen et al., 2021), and ice extent and surface properties (Gleason, 2006; Alonso-Arroyo et al., 2017; Cartwright et al., 2021; Roesler et al., 2021), vegetation biomass estimation (Egido et al., 2014; Santi et al., 2020; Pierdicca et al., 2021), Earth surface altimetry (Clarizia et al., 2016; Mashburn et al., 2018; Li et al., 2017, 2018; Cardellach et al., 2019; Wang and Morton, 2020; Nguyen et al., 2020; Zhang and Morton, 2023), etc. This study focuses on the precise measurement of water surface slope using GNSS signals coherently reflected off river surfaces. Preliminary case studies by Wang and Morton (2021b) and Wang and Morton (2022b) have demonstrated the feasibility of this application. Additionally, Warnock and Ruf (2019) and Warnock et al. (2024) have investigated river reflection signals to estimate river width and flow rate. In a low Earth orbit (LEO) at about 500 km altitude, the coherent reflection GNSS-R measurement has a footprint of ~500 m, as approximated by 0.6 times the first Fresnel zone for a homogeneous reflection surface (Camps, 2019), with a short along-track sampling spacing (such as 50 m for a 10-ms signal integration time). It offers high precision ranging measurement from carrier phase and the ability to penetrate cloud cover, precipitation, and vegetation. These characteristics of GNSS-R make it a valuable addition to current systems for inland water monitoring.

This paper further demonstrates the measurement of river slopes using GNSS-R by analyzing both raw intermediate frequency (IF) samples recorded by Cyclone GNSS (CYGNSS) satellites and grazing-angle GNSS-R data from Spire Global Inc. We specifically focus on river sections wider than approximately 500 m, which is close to the size of the GNSS-R footprint. Data segments are selected to measure surface slopes of the Amazon River and its tributaries, as well as the lower Mississippi River, as detailed in Section 2. These segments are selected to have diverse distributions in river width, track length, elevation angle, and geolocations, allowing for a comprehensive assessment of the effectiveness of GNSS-R in measuring river slopes under various

conditions. Section 3 documents the methodologies for measuring river slopes using GNSS-R, including altimetry retrieval, precise orbit determination, and open-loop (OL) processing of CYGNSS raw IF data. Section 4 details the mitigation of signal propagation errors, such as tropospheric delay and ionospheric effects, as well as an analysis of the error budget for river slope measurements by GNSS-R, considering additional error factors from reference surface heights and phase measurement noise. The processed river slope measurements from all selected data segments are validated by using nearby waterbodies that are expected to have almost zero surface gradients with respect to the geoid, such as lakes and off-channel river segments, and against gauge and satellite altimetry measurements in Section 5.

2. GNSS-R data

Major GNSS-R missions like TechDemoSat −1 (TDS-1) and CYGNSS are designed primarily for ocean scatterometry, producing delay-Doppler maps (DDMs) as their main outputs. While DDMs do not support river slope retrieval, both missions can capture a limited amount of raw IF data. This capability has facilitated the investigation of various scientific applications of GNSS-R. Moreover, Spire Global's CubeSat constellation, originally purposed for radio occultation, has been adapted for grazing-angle GNSS-R and recording 50 Hz in-phase (I) and quadrature (Q) correlation data for both direct and reflected GNSS signals in high latitudes and selected low-mid latitude areas. Future missions, such as HydroGNSS (Unwin et al., 2021), as well as commercial Earth observation constellations like those by PlanetiQ and Muon Space, are expected to offer additional GNSS-R measurements for applications to surface water observation.

The GNSS-R data used in this study includes the CYGNSS raw IF samples, which are freely accessible through NASA PO.DAAC, and Spire Global's grazing-angle GNSS-R data accessible to U.S. government funded investigators through the SmallSat Data Explorer: https://csdap.earthdata.nasa.gov/, with details introduced below.

2.1. CYGNSS raw IF

The CYGNSS constellation of eight microsatellites was launched in December 2016. Each CYGNSS satellite carries a GNSS-R receiver capable of tracking up to four simultaneous specular reflections of GPS L1 Coarse Acquisition (C/A) signals. The signals are received by two downward-looking antennas comprised of 2 × 3 planar phased arrays. Each antenna has a peak gain of 14 dBi with boresights aligned in the port and starboard cross-track directions at an off-nadir angle of 28°. Specular point (SP) reflections are measured over a range of angles of incidence from 0° (nadir) to ~70° (near the Earth limb), with the antenna gain decreasing to ~3 dBi at both boundaries. The wide off-nadir angular coverage, combined with the satellites' orbit inclination angle of 35°, results in sampling from 40°S to 40°N latitude.

The GPS L1 signal carrier frequency is 1575.42 MHz. The CYGNSS receiver downconverts the L1 signal to an IF frequency of 3.8724 MHz before digitizing it with a 2-bit resolution at a rate of 16.0362 MHz. In most cases, the raw data stream is processed in real-time to form DDM engineering data products. DDMs are formed by correlating the raw data with a local replica of the appropriate GPS pseudorandom noise (PRN) code, performing an initial coherent integration of the correlated voltage, and then performing a secondary incoherent integration of the squared voltage. Notably, DDM processing removes phase information contained in the raw data stream and averages the signal over 100 s of milliseconds, therefore it does not support GNSS-R phase altimetry or river slope retrieval. An alternative receiver operating mode is possible in which the raw IF data are stored directly, without additional processing, and then downlinked. This is a commanded mode which is reserved for observing targets of special interest, such as the river overpasses considered in this work. The on-board memory capacity of the CYGNSS spacecraft limits the length of raw IF data records to at most ~90 s. This corresponds to a ~500 km specular point track length. In practice, shorter data records are used to capture river overpasses since they are much narrower than the maximum track length.

2.2. Spire grazing-angle GNSS-R

The Spire grazing-angle reflections are collected opportunistically from nanosatellites originally designed for GNSS radio cccultation measurements. As of August 2024, up to 15 nanosatellites observe reflections at elevation angles ranging between 5 and 30 degrees. The nanosatellites are placed in sun-synchronous orbits at altitudes between 500 and 540 km and carry a software-defined science-grade GNSS receiver, STRATOS. This is a triple-frequency (L1, L2, L5) capable receiver. The receiver operationally processes GNSS signals from GPS, Galileo, GLONASS and Beidou constellations, although results in this paper are limited to GPS using the L1 C/A and L2 CL signals.

The STRATOS receiver connects to three antennas: one zenith-facing for precise orbit determination (POD) and two limb-facing (one fore, one aft), high-gain, three-patch right-handed circular polarization (RHCP) GNSS-RO antenna arrays. The antenna peak gains at L1 and L2 frequencies (1575 MHz and 1227 MHz) are 9.8 and 9.6 dBi, respectively. The 3 patches are combined with fixed electrical phasing to point down by 20 degrees to the Earth-limb.

The collections taken in this study used Spire's STRATOS Radio Frequency (RF) version 1 design. Each band starts with an input channel selection filter, then passes through a Low Noise Amplifier (LNA) and is then mixed to IF. At IF, it passes through a 2.5 MHz wide anti-aliasing filter, Automatic Gain Control (AGC), and then 2-bit ADC digitization at 6.2 MSPS. For the L2 band, the chain contains an additional mixer (after the LNA), to first convert the center frequency to the L1 band. The same RF design is then used for each band. The STRATOS reference clock is free-running, with some payloads using a high-quality temperature-compensated crystal oscillator (TCXO), and others utilizing a higher-stability oven-controlled crystal oscillator (OCXO).

The STRATOS receiver utilizes closed-loop tracking of the direct signals for the determination of position, velocity, and time. The science observables of direct and reflected signals are tracked using an OL model. For consistency, the exactly same OL approach is used for direct and reflected signals, with the difference being that the reflection path is modeled from the Earth's surface and includes twice the tropospheric delay model for Standard Point Positioning (RTCA (Firm). SC-159, 2006). The Earth surface model is selectable between the World Geodetic System 1984 (WGS84) ellipsoid or Earth Gravitational Model 2008 (EGM2008) geoid. The correlators start coherent integration from the signal's navigation bit transition boundary stored and downlinked as 50 Hz I and Q samples alongside the OL tracking model.

2.3. Selected GNSS-R datasets

This study selected 21 coherent reflection segments over the Amazon River and its tributaries from CYGNSS raw IF data collected during a raw IF data campaign from March to June 2021, along with 16 segments from Spire grazing-angle GNSS-R data (primarily from the same period). Among the Spire data segments, 15 are of signals reflected off the Mississippi River, and one is of signal reflected off the Tapajos River, one of the largest tributaries of the Amazon River. These datasets were collected or selected to have good spatial coverages of the Amazon and lower Mississippi River regions. The selected data segments and the corresponding river sections are summarized in Table 1. This table details the data files, time, geolocations (mean latitude and longitude of the SP tracks), elevation angle from the SP to the satellite, and the approximate SP track length and river width. The last column includes the reference river surface heights, which are interpolated using water level measurements from nearby gauges and/or Hydroweb virtual stations (Da Silva et al., 2010). These reference heights are used in the river slope retrieval process as further discussed in Section 3. The lengths of the selected river sections range from 1.5 to 99.9 km, with river widths between 0.6 and 19.1 km. These data segments and river sections are selected to have the GNSS-R SP at least ~200 m away from

Table 1
Summary of selected data segments and river sections from CYGNSS raw IF and Spire Global grazing angle GNSS-R data.

Track #	Dataset	PRN	Lat (°)	Lon (°)	El_{SP} (°)	Length (km)	Width (km)	Height (m)
C1	cyg05_raw_if_s20210326_213816_e20210326_213916	G11	−0.09	−50.00	12.15	8.9	11.9	1.0
C2	cyg01_raw_if_s20210612_082308_e20210612_082409	G31	−0.06	−50.22	27.55	19.0	19.1	1.0
C3	cyg03_raw_if_s20210325_205104_e20210325_205204	G28	0.23	−50.74	18.37	76.8	15.2	1.5
C4	cyg08_raw_if_s20210409_155300_e20210409_155401	G31	0.16	−50.80	34.51	99.9	15.2	1.5
C5	cyg01_raw_if_s20210612_082308_e20210612_082409	G31	−0.37	−50.71	27.07	8.3	9.8	2.0
C6	cyg05_raw_if_s20210326_213816_e20210326_213916	G11	−0.53	−50.78	11.30	10.8	11.8	2.0
C7	cyg06_raw_if_s20210603_124148_e20210603_124249	G21	−0.36	−51.37	76.95	17.0	2.7	2.5
C8	cyg05_raw_if_s20210326_213816_e20210326_213916	G11	−0.76	−51.19	10.84	4.7	4.5	2.5
C9	cyg03_raw_if_s20210423_075605_e20210423_075706	G10	−0.86	−52.51	46.50	2.1	0.6	5.3
C10	cyg01_raw_if_s20210612_082308_e20210612_082409	G26	−2.06	−54.01	35.01	9.7	8.0	7.7
C11	cyg01_raw_if_s20210612_082308_e20210612_082409	G26	−2.47	−54.58	34.85	4.5	4.0	9.6
C12	cyg06_raw_if_s20210603_124148_e20210603_124249	G04	−2.01	−55.85	47.72	14.4	4.1	12.4
C13	cyg04_raw_if_s20210603_132043_e20210603_132143	G22	−2.60	−56.83	35.85	5.5	4.5	15.1
C14	cyg05_raw_if_s20210503_045407_e20210503_045508	G12	−2.85	−58.07	41.04	19.5	4.6	17.5
C15	cyg05_raw_if_s20210503_045407_e20210503_045508	G12	−3.64	−59.04	40.64	12.0	1.7	20.6
C16	cyg08_raw_if_s20210603_130614_e20210603_130715	G01	−5.03	−59.35	69.12	8.5	2.9	20.7
C17	cyg08_raw_if_s20210603_130614_e20210603_130715	G01	−5.26	−59.65	69.36	7.8	0.6	20.9
C18	cyg06_raw_if_s20210409_034839_e20210409_034940	G24	−2.99	−60.55	51.75	37.8	13.6	23.3
C19	cyg03_raw_if_s20210603_015224_e20210603_015325	G24	−3.02	−60.54	71.50	22.3	13.6	21.0
C20	cyg07_raw_if_s20210423_093755_e20210423_093855	G18	−5.30	−60.63	17.96	2.4	1.1	29.2
C21	cyg07_raw_if_s20210503_033610_e20210503_033711	G32	−5.75	−63.58	10.03	1.5	0.5	36.8
S1	spire_gnss-r_L1B_grzRfl_v06.01_2021-05-23T09-58-12_FM117	G31	31.91	−91.21	29.10	2.5	1.8	21.0
S2	spire_gnss-r_L1B_grzRfl_v06.01_2021-06-12T09-47-05_FM104	G08	31.61	−91.40	26.21	3.0	1.0	18.0
S3	spire_gnss-r_L1B_grzRfl_v06.01_2021-05-05T23-40-23_FM117	G29	31.41	−91.48	28.74	3.7	1.6	18.5
S4	spire_gnss-r_L1B_grzRfl_v06.01_2021-05-15T10-13-06_FM106	G27	31.36	−91.49	9.20	7.1	1.1	17.5
S5	spire_gnss-r_L1B_grzRfl_v06.01_2021-05-25T17-10-12_FM125	G01	31.18	−91.60	25.44	5.4	1.2	15.4
S6	spire_gnss-r_L1B_grzRfl_v06.01_2021-05-08T16-26-16_FM099	G08	30.97	−91.66	17.99	4.7	0.9	14.0
S7	spire_gnss-r_L1B_grzRfl_v06.01_2021-05-18T02-54-02_FM102	G27	30.96	−91.66	15.07	4.0	0.9	14.8
S8	spire_gnss-r_L1B_grzRfl_v06.01_2021-03-15T23-28-50_FM117	G12	30.74	−91.47	11.97	3.3	0.7	12.5
S9	spire_gnss-r_L1B_grzRfl_v06.01_2021-06-24T03-40-16_FM116	G01	30.69	−91.35	10.01	4.4	1.2	9.9
S10	spire_gnss-r_L1B_grzRfl_v06.01_2021-04-29T16-57-24_FM124	G09	30.42	−91.20	7.27	4.3	0.9	9.7
S11	spire_gnss-r_L1B_grzRfl_v06.01_2021-06-24T04-06-37_FM128	G25	30.02	−90.72	29.85	3.2	0.6	4.5
S12	spire_gnss-r_L1B_grzRfl_v06.01_2021-03-04T06-47-05_FM128	G05	30.04	−90.60	20.01	5.4	0.7	3.6
S13	spire_gnss-r_L1B_grzRfl_v06.01_2021-05-03T04-31-43_FM125	G15	29.95	−90.06	27.80	1.6	0.6	3.3
S14	spire_gnss-r_L1B_grzRfl_v06.01_2021-05-29T19-27-32_FM128	G24	29.61	−89.87	19.81	10.4	0.7	1.4
S15	spire_gnss-r_L1B_grzRfl_v06.01_2020-11-15T03-14-59_FM102	G04	29.17	−89.26	9.92	6.9	1.4	0.2
S16	spire_gnss-r_L1B_grzRfl_v06.01_2020-04-14T06-44-02_FM105	G15	−2.89	−55.14	16.49	80.9	14.1	8.8

the riverbank, based on the satellite imagery data (such as Landsat) in Google Earth. The spatial distribution of the selected segments in Table 1 is visualized later in Fig. 7, where the yellow lines represent SP tracks from the CYGNSS raw IF data and the red ones represent those from Spire's grazing angle GNSS-R data. Also shown in the figures are the gauge and Hydroweb virtual stations that are used in this study. Additionally, several CYGNSS raw IF and Spire data segments were processed solely for phase noise performance analysis, as discussed in Section 4.4. These additional data segments are not included in Table 1 or Fig. 7.

There are some important distinctions between CYGNSS raw IF data and Spire grazing-angle GNSS-R data, summarized as follows: (1) The CYGNSS satellites record only the single-frequency L1 signal, meaning that the ionospheric effects must be mitigated using empirical models or ionospheric total electron content (TEC) data products, rather than the, more accurate, dual-frequency ionosphere correction. Any uncorrected ionospheric refraction can lead to significant errors in GNSS-R river slope retrieval (Wang and Morton, 2021a). In contrast, Spire's satellites process both L1 and L2 signals, allowing for accurate estimation and correction of ionospheric effects. (2) CYGNSS satellite orbits have a lower inclination angle of approximately 35°, making them more suitable for observing east–west river sections rather than north-south river sections. In contrast, the Spire data used in this study primarily come from LEO satellites in near-polar orbits, which are advantageous for observing rivers oriented more in the north-south direction. (3) CYGNSS satellites are equipped with two left-hand circular polarization (LHCP) phased-array antennas, capturing all visible signals from a wide range of directions with an antenna gain of up to 14 dBi. Spire's satellites carry two RHCP phased-array antennas, making the actual antenna gain for receiving river-reflection signals (mostly left-hand circularly polarized) unclear. Due to the limited beamwidth of their antennas, Spire's satellites only process signals reflected at elevation angles (from SP to GNSS) ranging from about 5° to 30°. The antenna polarization, gain patterns, and off-boresight angles directly affect the noise level of signal measurements. (4) The CYGNSS raw IF data is at a lower processing level and requires further processing for signal carrier phase estimation, typically through OL tracking. Such low-level data also provides opportunities to test GNSS-R signal processing algorithms and evaluate their impact on scientific retrieval performance. Spire satellites process the GNSS-R signals onboard with OL tracking and generate 50-Hz I and Q correlator outputs in the data products.

Analyzing data from both sources will provide valuable insights for future instrument and mission designs aimed at processing coherent reflection GNSS-R signals and advancing GNSS-R in inland water observation and other altimetry applications.

3. Methodology

The river slope retrieval is based on GNSS-R carrier phase-based altimetry, and an illustration is shown in Fig. 2, where a LEO satellite receives signals directly from the GNSS satellite and signals reflected off the river surface. With precisely estimated orbit and clock information of both the transmitting (GNSS) and receiving (LEO) satellites and a surface elevation model, the signal reflection geometry and path length can be modeled (shown as dashed orange line in Fig. 2), and the actual reflection path (solid orange line) is precisely measured by the receiver using reflected signal carrier phase. Note that the carrier phase only offers a relative range measurement, meaning it only measures changes in path length, without phase-to-pseudorange leveling. The GNSS-R excess phase, which is defined as the residual carrier phase measurement after subtracting the geometric range model, atmospheric

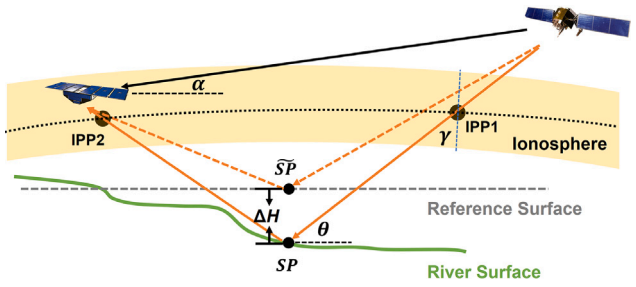


Fig. 2. Illustration of GNSS-R altimetry on a LEO satellite. SP: Specular point. IPP: Ionopsheric pierce point. (For interpretation of the references to color in this figure legend, the reader is referred to the web version of this article.)

delay, and ionospheric effects, predominantly represents the vertical variation of the SP and can be used to measure the relative surface heights along the SP track.

The reference surface height is important for the accurate modeling of GNSS-R geometry and therefore impacts the river slope retrieval accuracy. Ideally, it should be modeled or estimated with approximately 1 m or better accuracy, corresponding to ~0.24 cm/km river slope error, as analyzed later in Section 4.1 and Table 1. In this paper, we use interpolated water level measurements from nearby gauge stations and/or Hydroweb virtual stations (derived from satellite altimetry), as listed in Table 1, and these reference surface heights are with respect to the EGM2008 geoid (Pavlis et al., 2012). When such water level measurements are not available, less accurate options include the SWOT Mission River Database (SWORD, Altenau et al. (2021)) and digital elevation models (DEM) such as the Shuttle Radar Topography Mission (SRTM) DEM (Farr et al., 2007).

3.1. GNSS-R phase altimetry

This subsection provides a more detailed and mathematical representation of GNSS-R phase altimetry. We will use the accent mark ^ to denote measured and post-processing estimation of variables, ~ to denote modeled and a prior estimates of variables, and no accent marks for true states or constants. Subscripts D and R are used to denote variables associated with the direct and reflected signals, respectively.

The GNSS-R receiver estimates the coherently reflected signal carrier phase $\hat{\phi}_{\mathrm{R}}$ at receiver time $\hat{t}_{\mathrm{rx}}$ (with clock bias corrected). Here the unit of radians is used for carrier phase ϕ. After converting the unit to seconds by dividing by the GNSS carrier frequency ω_c in radians per second, $\hat{\phi}_{\mathrm{R}}/\omega_c$ represents the relative transmission time of the signal (with an unknown and constant offset), and it includes the GNSS satellite clock bias b_{tx}. Accurate estimation of b_{tx} is available from data processing centers, such as International GNSS Service (2010) (IGS). There is usually a navigation module along with or integrated into the GNSS-R receiver that provides position, velocity, and timing (PVT) information of the receiver and raw pseudorange and carrier phase measurements of direct line-of-sight (LOS) signals. These measurements are further processed to obtain the LEO satellite orbit and clock solutions. The reflected signal propagation range can be estimated from these solutions:

$$\hat{\rho}_{\mathrm{R}}(t_{\mathrm{rx}}) = \hat{b}_{\mathrm{rx}}(\hat{t}_{\mathrm{tx}}) \cdot c - \hat{\boldsymbol{\Phi}}_{\mathrm{R}}(\hat{t}_{\mathrm{rx}}) + \hat{b}_{\mathrm{tx}}(\hat{t}_{\mathrm{tx}}) \cdot c + const. \tag{1}$$

where $\hat{t}_{\mathrm{rx}}$ is receiver time and b_{rx} is the receiver clock bias. For convenience, $\boldsymbol{\Phi} = \phi \cdot c/\omega_c$, in meters, is introduced in the following equations, with c being the speed of light. The reflected signal carrier phase is measured as $\hat{\boldsymbol{\Phi}}_{\mathrm{R}}$ at centimeter precision, and again, with an unknown and constant offset. Here the signal transmission time $\hat{t}_{\mathrm{tx}}$ is estimated based on the propagation time and iteratively to account for the Earth rotation.

The estimated reflected signal propagation range from Eq. (1) consists of the GNSS-SP-LEO geometric range, ionospheric effects, tropospheric delay, and other factors such as multipath and noise, and it can be modeled as:

$$\begin{aligned}\tilde{\rho}_{\mathrm{R}}(\hat{t}_{\mathrm{rx}}) = {} & |\hat{\mathbf{r}}_{\mathrm{tx}}(\hat{t}_{\mathrm{tx}}) - \hat{\mathbf{r}}_{\mathrm{sp}}(\hat{t}_{\mathrm{rx}})| \\ & + |\hat{\mathbf{r}}_{\mathrm{sp}}(\hat{t}_{\mathrm{rx}}) - \hat{\mathbf{r}}_{\mathrm{rx}}(\hat{t}_{\mathrm{rx}})| + \hat{I}_{\mathrm{R}}(\hat{t}_{\mathrm{rx}}) + \hat{T}_{\mathrm{R}}(\hat{t}_{\mathrm{rx}})\end{aligned} \tag{2}$$

where subscript R denotes reflected signal, $\mathbf{r}_{\mathrm{tx}}$, $\mathbf{r}_{\mathrm{sp}}$, $\mathbf{r}_{\mathrm{rx}}$ are the Earth-Centered, Earth-Fixed (ECEF) coordinate vectors of the GNSS satellite, SP, and LEO satellite, respectively, I represents the ionospheric effects on carrier phase. Note that to the first order approximation, the ionosphere has opposite effects on carrier phase and pseudorange but same magnitudes in meters (Morton et al., 2020), and T represents the tropospheric delay. The estimation and/or modeling of I and T are introduced in Section 4. The SP coordinates are estimated through a minimum-path-length method (Gleason, 2010):

$$\underset{\hat{\mathbf{r}}_{sp}}{\operatorname{argmin}} f(\mathbf{r}_{sp}) = | \mathbf{r}_{rx} - \mathbf{r}_{sp} | + | \mathbf{r}_{sp} - \mathbf{r}_{tx} | \tag{3}$$

and the SP is constrained to the reference surface height $\tilde{H}$.

Another factor that needs to be addressed is the receiver clock error, which typically introduces fluctuations of centimeters or more in GNSS carrier phase measurements in addition to its lower-frequency drifts. These fluctuations are not accounted for by the standard 1 Hz receiver clock solution. One effective approach to mitigate this error is by estimating the clock-induced phase fluctuations using the direct GNSS signal at a higher sampling rate. For example, Spire CubeSats process both direct and reflected signals for their grazing-angle GNSS-R products. Such fluctuations, denoted by $\delta\hat{\boldsymbol{\Phi}}_{osci}$, are estimated using the following set of equations:

$$\hat{\rho}_{\mathrm{D}}(t_{\mathrm{rx}}) = \hat{t}_{\mathrm{rx}} \cdot c - \hat{\boldsymbol{\Phi}}_{\mathrm{D}}(\hat{t}_{\mathrm{rx}}) + b_{\mathrm{tx}}(\hat{t}_{\mathrm{rx}}) \cdot c + const. \tag{4}$$

$$\tilde{\rho}_{\mathrm{D}}(\hat{t}_{\mathrm{rx}}) = |\hat{\mathbf{r}}_{\mathrm{tx}}(\hat{t}_{\mathrm{tx}}) - \hat{\mathbf{r}}_{\mathrm{rx}}(\hat{t}_{\mathrm{rx}})| + \hat{I}_{\mathrm{D}}(\hat{t}_{\mathrm{rx}}) \tag{5}$$

$$\delta\hat{\boldsymbol{\Phi}}_{osci}(\hat{t}_{\mathrm{rx}}) = \hat{\rho}_{\mathrm{D}}(\hat{t}_{\mathrm{rx}}) - \tilde{\rho}_{\mathrm{D}}(\hat{t}_{\mathrm{rx}}) \tag{6}$$

where the variables are defined the same way as in Eqs. (1), (2), and subscript D denotes variables associated with the direct signal.

Then the reflected signal excess phase, which primarily corresponds to the vertical variations in the reflection surface heights, can be obtained as

$$\delta\hat{\boldsymbol{\Phi}}_{s}(\hat{t}_{\mathrm{rx}}) = \hat{\rho}_{R}(\hat{t}_{\mathrm{rx}}) - \tilde{\rho}_{R}(\hat{t}_{\mathrm{rx}}) - \delta\hat{\boldsymbol{\Phi}}_{osci}(\hat{t}_{\mathrm{rx}}) \tag{7}$$

and the relative river surface deviations from the reference height are then retrieved through

$$\Delta\hat{H}(\hat{t}_{\mathrm{rx}}) = -\frac{\delta\hat{\boldsymbol{\Phi}}_{s}(\hat{t}_{\mathrm{rx}}) - \delta\bar{\boldsymbol{\Phi}}_{s}(\hat{t}_{\mathrm{rx}})}{2\sin\theta(\hat{t}_{\mathrm{rx}})} \tag{8}$$

where θ is the elevation angle from SP to GNSS or LEO satellite, as shown in Fig. 2, and $\delta\bar{\boldsymbol{\Phi}}_{s}$ is the mean value of $\delta\hat{\boldsymbol{\Phi}}_{s}$. If $\Delta\hat{H}$ is observed to have steep gradients, an additional iteration can be applied to the retrieval, i.e., replace $\tilde{H}$ with $\hat{H}$ and repeat the processes in Eqs. (2), (3), (7), (8). Then the river slope is based on the retrieved relative river surface heights $\hat{H} = \tilde{H} + \Delta\hat{H}$, with examples shown in Fig. 7.

The GNSS-R phase altimetry method as introduced above requires input of carrier phase measurement $\hat{\boldsymbol{\Phi}}$ (of both direct and reflected signals) and POD solutions for the LEO satellite. This method is directly applicable to Spire's grazing-angle GNSS-R data, such as Level 1B grzRfl, which provides carrier phase measurements with navigation data bits removed. To retrieve river slopes from CYGNSS raw IF data, additional POD processing and OL tracking are required.

The block diagram in Fig. 3 illustrates a complete data processing flow for using spaceborne GNSS-R to retrieve river slope. In addition to "Altimetry Retrieval", this block diagram also includes the RF front-end signal processing, navigation solutions, POD, and carrier phase estimation through OL tracking. The Zenith and Nadir RF Front-ends

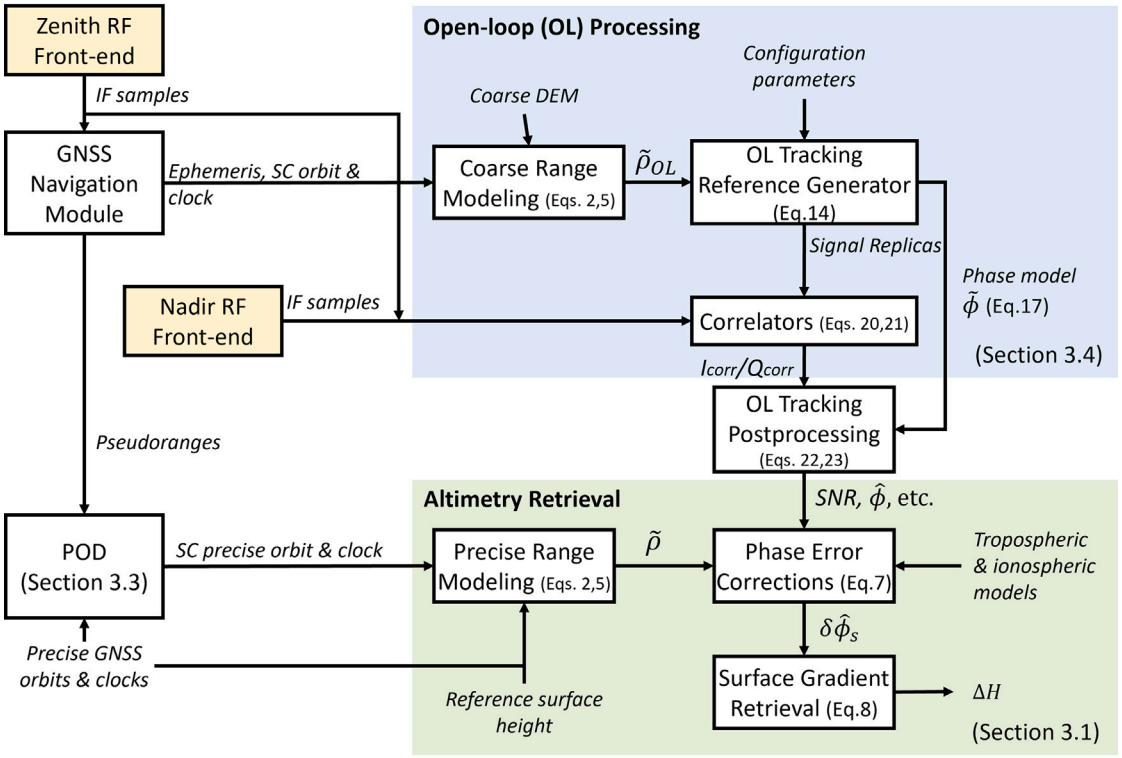


Fig. 3. Block diagram of coherent-reflection GNSS-R signal processing and carrier phase-based altimetry retrieval.

consist of components such as amplifier, filter, down-converter, digital sampler, etc. They are connected to an upward-looking RHCP antenna and a downward- or side-looking LHCP or RHCP antenna, respectively. The Zenith RF Front-end outputs IF data samples to the "GNSS Navigation Module", which is usually a commercial off-the-shelf (COTS) GNSS receiver onboard satellites. The COTS GNSS receiver typically provides 1-Hz navigation solutions, which can be used in real-time for the DDM processing or OL tracking, and it also records the raw measurements of pseudorange and carrier phase, which can be further processed for POD. Both RF Front-ends receive, down-convert, and digitize GNSS signal to IF samples. The IF samples are processed through OL tracking to generate I and Q correlator outputs (denoted as $I_{\text{corr}}/Q_{\text{corr}}$ in Fig. 3), which are further processed in "OL Tracking postprocessing" for the estimation of carrier phase $\hat{\Phi}$.

More details of POD and OL processing for using the CYGNSS raw IF data are discussed below in Sections 3.3 and 3.4, respectively.

3.2. River slope estimation

The river slope estimation follows the "$\partial h/\partial x$" definition, as used by Alsdorf et al. (2007) and Paz and Collischonn (2007). The GNSS-R river slope is determined based on the phase altimetry, i.e., the retrieval of the relative WSE along the SP track, with respect to the geoid. As illustrated in Fig. 1, the river slope is estimated as:

$$slope = \frac{\hat{H}_{up} - \hat{H}_{down}}{D_{centerline}} \tag{9}$$

where $\hat{H}_{up}$ and $\hat{H}_{down}$ represent the retrieved relative WSE (after noise filtering) of the upstream and downstream ends, respectively, of the selected GNSS-R SP track over the river surface, and $D_{centerline}$ is the distance of the river centerline between the upstream and downstream points. For each GNSS-R track, $D_{centerline}$ is manually delineated and measured on satellite images in Google Earth.

For relatively short segments of GNSS-R altimetry retrievals exhibiting a linear trend, filtering is applied using a linear fit to $\hat{H}$. For longer segments, $\hat{H}_{up}$ and $\hat{H}_{down}$ are computed as the average of five samples at each end of the GNSS-R SP track. Detailed examples are provided in Section 5 and illustrated in Fig. 7(c) and (d).

3.3. Precise orbit determination

Precise orbits are not available as standard CYGNSS data products, however, with the addition of GPS pseudorange and carrier phase in the telemetry record, a POD method has recently been implemented that can provide orbit quality to support this application.

The SSTL SGR-ReSI receivers onboard the CYGNSS satellites report navigation (NAV) solutions in real-time at a 1-Hz rate. These point-solutions are based on noisy, single-frequency pseudorange measurements and GPS broadcast ephemeris data, without incorporating dynamical orbit modeling. The resulting solutions are further truncated to 1 m precision in the telemetry stream for a final 1σ 3-D position error of about 3 m. While this level of orbit quality is sufficient to support the CYGNSS mission's ocean surface wind retrievals, for altimetry applications, precise GNSS-based orbit determination incorporating carrier phase observations and detailed dynamical models is required.

Conrad et al. (2023) developed and demonstrated a POD approach for CYGNSS, using the Jet Propulsion Laboratory (JPL) GipsyX software (Bertiger et al., 2020) to process single-frequency pseudorange and carrier phase data. The pseudorange and carrier phase measurements are combined into a GRoup And PHase Ionosphere Correction (GRAPHIC) observable (Yunck, 1993; Montenbruck, 2003) computed from the navigation receiver output of GPS L1 C/A pseudorange ρ_{nav} and carrier measurements Φ_{nav} as:

$$GRAPHIC = \frac{\rho_{\text{nav}} + \Phi_{\text{nav}}}{2} \tag{10}$$

$$\rho_{\text{nav}} = r + b_{\text{nav}} + I + \epsilon_{\rho} \tag{11}$$

$$\Phi_{\text{nav}} = r + b_{\text{nav}} - I + N + \epsilon_{\Phi} \tag{12}$$

where r is the geometric range, b_{nav} is the receiver clock bias, N is the carrier phase ambiguity, and ϵ represents noise and other errors, and I represents the delay due to the ionosphere. The GRAPHIC

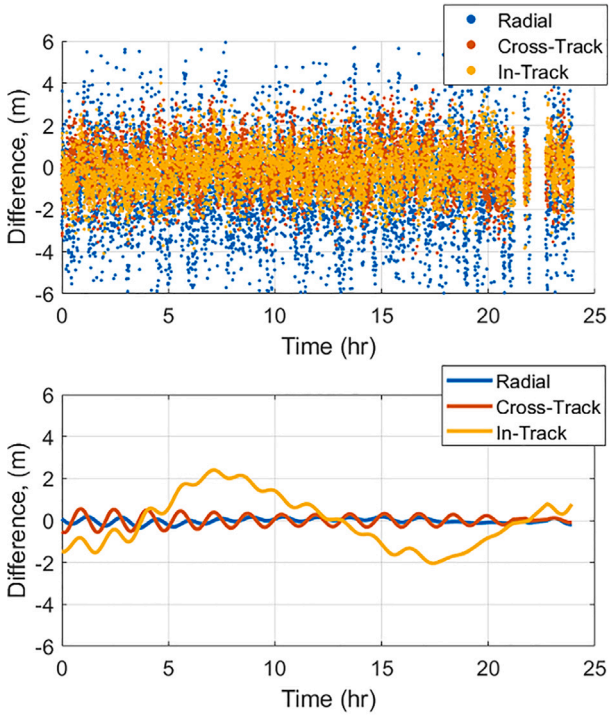


Fig. 4. Time history of the radial, cross-track, and in-track component differences between the GipsyX GRAPHIC post-processed POD solution and the onboard NAV solution (top) and dynamic orbit solution fit to the NAV data (bottom) for March 25, 2021.

combination creates an ionosphere-free observable with a half-integer cycle ambiguity and half the code noise. An additional measurement adjustment is required in working with CYGNSS data to remove a clock-like divergence between the code and carrier data. Then daily reduced dynamic CYGNSS orbit estimates are generated for 30-h arcs centered on noon each day. The dynamic models used in GipsyX include solar (Milani et al., 1987) and earth radiation pressure forces (Knocke et al., 1988), drag (Bruinsma et al., 2003) time-variable gravity, ocean tides, solid earth tides, pole tides, and third-body effects. A CYGNSS GPS zenith antenna calibration is also estimated from the in-flight data and applied to correct for systematic effects such as multipath. With these techniques, Conrad et al. (2023) demonstrated an orbit overlap precision of 1.4 cm radial, 1.2 cm cross-track, and 3.0 cm in-track with an expected overall orbit accuracy of 2.8 cm radial, 2.4 cm cross-track, and 6 cm in-track.

For times when GPS pseudorange and phase measurements are not available, some improvement can still be gained by fitting a dynamic orbit to the NAV solutions. The GipsyX POD solution process does this during the first step, and a direct comparison of the dynamic fit can be made to the GRAPHIC POD solution. Fig. 4 shows the time history of the component differences between this dynamic fit and the POD solution. The component difference rms values are 0.12 m for radial, 0.26 m cross-track, and 1.3 m in-track, resulting in a total 3D difference rms of 1.3 m. These dynamic orbits are much better than the original NAV solution. However, the GipsyX POD solution is preferred given the previously described orbit overlap performance, smaller GRAPHIC daily residual rms (0.5 m) when compared to the NAV solution residual rms (3 m), and the reduced dynamics in combination with the ionosphere-free GRAPHIC observable.

The impact of orbit errors on river slope measurement is predominantly due to its variations rather than the absolute error magnitudes. Given the centimeter accuracy of POD solutions, such impact should be minimal. Instead of using the GipsyX software, a simplified approach is adopted to fit CYGNSS orbits for the selected datasets in this study. A 6th-order polynomial fit is applied to 20 min of the CYGNSS NAV solutions provided in the Level 1 product. The precise orbit of CYGNSS #03 satellite on March 25, 2021 was generated based on the POD methods presented above for validation. The maximum and RMS values of the orbit error gradients from the 6th-order polynomial fit are 2.4 and 1.1 cm/s, respectively. An orbit error gradient of 1.1 cm/s leads to a fractional error of 0.2 cm/km in river slope measurement, considering an average SP speed of 5 km/s and the geometric projection of orbit errors. Therefore, POD is necessary to achieve the most accurate GNSS-R measurements of river slope and the 6th-order polynomial fit, yielding sub-cm/km orbit gradient errors, is also effective from the perspective of demonstrating the GNSS-R performance in this paper. For river slope measurements from Spire grazing-angle GNSS-R data, the impact of orbit errors is minimal, as the retrieval uses Spire POD solutions with an accuracy of approximately 10 cm.

3.4. GNSS-R carrier phase estimation

The GNSS-R signal carrier phase is usually estimated through OL types of processing. For example, Spire satellites conduct onboard OL tracking of the pair of direct and reflected GNSS signals with early-prompt-late correlators, which enable the estimation of both pseudorange and carrier phase. The conventional closed-loop tracking is effective for estimation of reflected signal carrier phase in controlled case studies (Wang and Morton, 2019). However, it is not suitable for onboard processing due to the unpredictable and highly variable coherence level of the reflected signals, particularly over land, where a coherent reflection segment for inland water can be as short as tens of milliseconds. OL processing methods for CYGNSS raw IF data have been documented by, for example, Li et al. (2019) to produce complex waveforms, Wang and Morton (2020) with early-prompt-late correlations, and Wang and Morton (2022a) for complex DDM processing of signals reflected over complex terrains, such as glaciers, with more correlators to account for the increased OL model uncertainty.

In this work, as solely carrier phase and no pseudorange is used for retrieving river slopes, the early-prompt-late and additional correlations are not necessary. Therefore, a single pair of prompt in-phase and quadrature correlations is employed in the OL processing of direct and reflected signals, respectively.

The GNSS IF signal can be represented as

$$s(t) = A \cdot D(t-\tau) \cdot C(t-\tau) \cdot \cos(\omega_{\mathrm{IF}} t + \phi) + \epsilon \tag{13}$$

where t is the signal reception time, variables A, τ, ϕ, ϵ are the signal amplitude, signal propagation time, baseband carrier phase, and noise, respectively, D and C are sequences of navigation date bit and PRN code, respectively, and ω_{IF} is a known constant of intermediate frequency in radian. The OL processing here aims to estimate baseband carrier phase Φ_{D} and Φ_{R}, as introduced in Eqs. (1), (4), and it is through the correlation between samples of the received IF signal and locally modeled replica signal. Modeling the replica signal follows:

$$r(t) = C(t-\tilde{\tau}) \cdot \exp[j(\omega_{\mathrm{IF}} t + \tilde{\phi})] \tag{14}$$

where receiver time t is estimated in real-time in the navigation processing, here denoting the estimates as $\hat{t}_{\mathrm{rx}}$, and the receiver clock bias has been corrected.

The signal propagation time τ is modeled as:

$$\tilde{\tau}_D(\hat{t}_{\mathrm{rx}}) = \hat{t}_{\mathrm{rx}} + \hat{b}_{\mathrm{tx}}(\hat{t}_{\mathrm{tx,D}}) - \tilde{\rho}_{\mathrm{D,OL}}(\hat{t}_{\mathrm{rx}})/c \tag{15}$$

$$\tilde{\tau}_R(\hat{t}_{\mathrm{rx}}) = \hat{t}_{\mathrm{rx}} + \hat{b}_{\mathrm{tx}}(\hat{t}_{\mathrm{tx,R}}) - \tilde{\rho}_{\mathrm{R,OL}}(\hat{t}_{\mathrm{rx}})/c \tag{16}$$

where GNSS satellite clock bias $\hat{b}_{\mathrm{tx}}$ is calculated from the ephemeris data decoded along with the navigation solution, $\tilde{\rho}_{\mathrm{D,OL}}$ and $\tilde{\rho}_{\mathrm{R,OL}}$ are modeled similarly as in Eqs. (5) and (2), respectively, and slight differences are that the satellite orbit and clock solutions are solved in real-time by the onboard receivers instead of through postprocessing and that modeling the atmospheric effects is usually not necessary in

OL tracking.

For higher precision, ϕ is modeled based on the real-time estimated receiver velocity, instead of position:

$$\tilde{\phi}(t) = \int_0^t \tilde{\omega}(t)dt + \phi_0 \tag{17}$$

$$\tilde{\omega}_{\mathrm{D}} = \frac{\omega_{\mathrm{RF}}}{c} \cdot \{[\hat{\mathbf{v}}_{\mathrm{tx}} - \hat{\mathbf{v}}_{\mathrm{rx}}] \cdot \hat{\mathbf{u}}_{\text{tx-rx}} + \hat{\dot{b}}_{\mathrm{rx}}\} \tag{18}$$

$$\tilde{\omega}_{\mathrm{R}} = \frac{\omega_{\mathrm{RF}}}{c} \cdot [\hat{\mathbf{v}}_{\mathrm{tx}} \cdot \hat{\mathbf{u}}_{\text{tx-sp}} - \hat{\mathbf{v}}_{\mathrm{rx}} \cdot \hat{\mathbf{u}}_{\text{sp-rx}} + \hat{\dot{b}}_{\mathrm{rx}}] \tag{19}$$

where ω is Doppler frequency in radian per second, and it is modeled based on the real-time estimated receiver velocity $\hat{\mathbf{v}}_{\mathrm{rx}}$, receiver clock bias rate $\hat{\dot{b}}_{\mathrm{rx}}$, unit LOS vectors $\hat{\mathbf{r}}$, and the decoded GNSS satellite velocity $\hat{\mathbf{v}}_{\mathrm{tx}}$. The information can be obtained from the CYGNSS level-1 data product or using GPS broadcast ephemeris if working with the raw IF data.

The generated replica signal $r(t)$ is correlated with the received signal $s(t)$ to generate the in-phase and quadrature correlation outputs:

$$I_k = \int_{(k-1)T_c}^{kT_c} \mathrm{Re}[r(t) \cdot s(t)]dt \tag{20}$$

$$Q_k = \int_{(k-1)T_c}^{kT_c} \mathrm{Im}[r(t) \cdot s(t)]dt \tag{21}$$

where T_c is the coherent integration time in the tracking loop and k is a discrete time tag. The coherent integration usually starts at the boundary between data bit transitions and does not exceed 20 ms, unless the navigation bits are modulated in the replica signal.

Defining the carrier phase error as $\delta\boldsymbol{\Phi} = \tilde{\boldsymbol{\Phi}} - \boldsymbol{\Phi}$, the discrete-time phase measurements at a rate of $1/T_c$ can be obtained by applying a four-quadrant phase discriminator:

$$\delta\boldsymbol{\Phi}_k = \mathrm{atan2}(Q_k, I_k) \cdot \lambda/(2\pi) \tag{22}$$

$$\hat{\boldsymbol{\Phi}}_k = \tilde{\boldsymbol{\Phi}}_k + \delta\boldsymbol{\Phi}_k + n_k\lambda + m_k\lambda/2 \tag{23}$$

where m, n are integers, $n\lambda$ is the unwrapping term of full cycles, and $m\lambda/2$ are the half-cycle phase jumps due to data bit transitions. $m\lambda/2$ will not be present if the navigation data bits are modulated to the replica signal $r(t)$ before correlation.

In the postprocessing of OL tracking outputs, navigation data bits D can be obtained from external sources, such as the *bitarc* product produced by UCAR COSMIC Program. It can also be estimated in a simpler way by detecting half-cycle phase jumps in the direct signal phase measurement $\hat{\boldsymbol{\Phi}}_{\mathrm{D}}$, assuming the direct signal is clean and healthy. Then the half-cycle phase jumps can be removed from both direct and reflected phase by

$$\delta\phi_k = \mathrm{atan2}(Q_k \cdot D_k, I_k \cdot D_k) \tag{24}$$

After the correction of half-cycle phase jumps, n is selected from $\{-1, 0, 1\}$ by minimizing $|\hat{\phi}_k - \hat{\phi}_{k-1}|$ to unwrap phase measurements $\hat{\phi}$ (Sokolovskiy, 2001).

If the carrier phase measurements are noisy, it can be challenging to accurately unwrap them, potentially leaving some cycle slips undetected or mis-corrected. Here a modified simultaneous cycle-slip and filtering (SCANF) method (Wang et al., 2020) is used for cycle slip correction, and the modification is to retain the phase noise to avoid over-filtering. Therefore, unless specified in the figures or captions, all other river slope retrievals presented in this paper used unfiltered carrier phase.

4. Error mitigation and analysis

This section focuses on mitigating and analyzing primary error sources in spaceborne GNSS-R river slope measurements. Key error terms examined here include the modeling of reflection geometry, ionospheric effects, tropospheric delay, and phase noise. Understanding and effectively addressing these sources of error is crucial for achieving precise river slope measurements with quantified uncertainty.

The river slope measurement is derived from GNSS-R phase altimetry, which outputs relative water surface heights. The emphasis on relative heights means that the primary factors impacting the river slope measurement accuracy are the variations of error terms, rather than their absolute magnitudes. Consequently, for some error factors that are significant in the construction of reflection geometry for absolute altimetry (e.g., Mashburn et al. (2018)), their variations are negligible for short GNSS-R segments ranging from fractions of a second to a few seconds used for river slope retrieval. These error terms include antenna phase center offsets, satellite attitude variations (if there are no sudden maneuvers), and solid Earth tide effects. In this section, regarding the modeling of GNSS-R geometry, two major error factors from orbit solutions and reference surface heights are analyzed in Section 4.1.

As GNSS signals traverse through the ionosphere and troposphere, carrier phase-based ranging measurements capture ionospheric phase advances and tropospheric delay effects, which can exhibit notable variations even over short intervals. Phase noise constitutes another significant source of uncertainty in river slope measurements, particularly for short river-reflection segments. These three major error terms are discussed in details in the following Sections 4.2 to 4.4 and further summarized in Section 4.5.

In addition to the more "systematic" measurement errors as mentioned above, GNSS-R river slope measurements may be influenced by additional factors that can contribute to inaccuracies. These include ocean tidal effects near river mouths, superelevation effects at curved sections, multipath interference from nearby water bodies with different water surface heights from the river channel, etc. While these factors are not analyzed in this section, they are discussed in relation to their impact on the results in Section 5.

4.1. Geometry modeling

Given the expected overall orbit accuracy of 5 cm (radial) from POD and the dynamic orbit fit assessment shown in Fig. 4 (bottom panel, maximum error gradient of ~0.04 cm/km), the impact of orbit errors on river slope is considered to be minimal, at around 0.01 cm/km. With the absence of POD solutions, using a simple polynomial fit to the real-time orbit solutions, a 0.2 cm/km error in river slope is expected at 30° elevation angle (as discussed earlier in Section 3.3).

The estimation of SP represents another significant error source in GNSS-R geometry modeling. This section focuses specifically on the impact of vertical deviations in SP, which refer to errors in the reference surface heights used to constrain SP estimation in Eq. (3). As discussed in Section 3, we utilize interpolated water level measurements from nearby gauge stations and/or Hydroweb virtual stations as reference surface heights. In our analysis of their impact, these reference surface heights are assumed to have a standard deviation of 1 m. This analysis is statistically conducted based on the orbit of CYGNSS #03 satellite on March 25, 2021. Specifically, we begin by modeling the reflected path ranges for all GPS signals received by the CYGNSS satellite throughout the day, assuming coherent reflection from the WGS84 ellipsoid. Subsequently, we simulate a scenario where the WGS84 ellipsoid is lowered by 1 m and compute the resulting differences in reflected path ranges. These differences, spanning an elevation angle range of 10° to 70°, exhibit gradients with a standard deviation of 1.22 cm/s. This corresponds to an approximate error of 0.24 cm/km in river slope estimation at 30° elevation angle (assuming a velocity of SP of 5 km/s).

4.2. Ionosphere

The ionosphere is a weakly ionized layer of the Earth's atmosphere filled with charged particles. The varying electron density within

the ionosphere significantly impacts radio waves traveling through it, causing effects such as group delay, phase advance, refraction, and, occasionally, diffraction, all of which are frequency-dependent. In GNSS-R phase altimetry and river slope measurement, ionospheric effects predominantly manifest as a phase advance, which can be approximated based on the first-order term in the Appleton-Hartree equation of refractive index, and it is proportional to TEC/f^2 (Morton et al., 2020). The calculation of phase advance follows:

$$TEC = \frac{f_1^2 f_2^2}{40.3(f_1^2 - f_2^2)} \left(\hat{\Phi}_2 - \hat{\Phi}_1\right) + const. \tag{25}$$

$$\hat{I} = \frac{40.3TEC}{f^2} \tag{26}$$

where TEC is a measure of the total number of electrons present in a column of the ionosphere with a cross-sectional area of 1 square meter, along the signal propagation path and extending from the receiver to the edge of the ionosphere, $\hat{I}$ denotes the estimated relative ionospheric phase advance, f_1 and f_2 are the frequencies of the two carrier signals, and subscripts 1 and 2 denote variables corresponding to these two frequencies, respectively. Both I and Φ here are in meters. This dual-frequency estimation of relative ionospheric phase advance is precise to mm-level under quiet ionospheric conditions and may reach cm-level during solar-geomagnetic storms (Morton et al., 2009). The residual ionospheric error in the river slope retrieval is therefore minimal, since only the gradient in the residual error needs to be considered.

CYGNSS only has single-frequency measurement capabilities. Therefore, the ionospheric TEC cannot be estimated using dual-frequency measurements as in Eq. (25). Instead, TEC is obtained from external sources, such as the Global Ionosphere Map (GIM) and the Madrigal database (Rideout and Coster, 2006). GIMs, for example, produced by Jet Propulsion Laboratory (JPL) (Martire et al., 2024), are global TEC maps generated based on measurements from hundreds of GNSS receivers and climatological models to aid areas with poor data coverage. In contrast, the Madrigal database uses purely GNSS measurements from approximately 6000 GNSS receivers to produce TEC maps with a 1° × 1° spatial resolution and a 5-min cadence. However, it has blank areas that have no data coverage. Most of the river slope results from CYGNSS raw IF data in this paper are retrieved using TEC from Madrigal, with a few cases using GIMs in the absence of Madrigal data.

The GIMs and Madrigal TEC maps are vertical TEC maps typically based on a single-shell ionospheric model, which assumes that all ionospheric electrons are concentrated in a thin shell located at approximately 350–450 km altitude. As illustrated in Fig. 2, the reflected GNSS signal intersects with the abstract ionosphere shell (dashed black line) at two ionospheric pierce points (IPP), IPP1 and IPP2, for the incidence ray and reflection ray, respectively. An obliquity factor or a mapping function $1/\cos(\eta)$ is then applied to convert the vertical TEC ($vTEC$) obtained from GIM or Madrigal TEC maps to slant TEC ($sTEC$), providing an approximation of the TEC along the reflected signal's propagation path:

$$sTEC_{\mathrm{R}} = \frac{vTEC_{\mathrm{IPP1}} + \beta \cdot vTEC_{\mathrm{IPP2}}}{cos(\eta)} \tag{27}$$

where η is the elevation angle from the incidence ray IPP to the GNSS satellite, and β denotes the proportion of TEC below the orbit height and can be obtained from an ionospheric model (Wang and Morton, 2021b), such as the international reference ionosphere (IRI) (Bilitza, 2018).

As explained in Section 3.1, the receiver oscillator fluctuations are estimated using the direct signal carrier phase. Therefore, the ionospheric effect on the direct signal also needs to be estimated. With dual-frequency measurements, the estimation follows Eqs. (25), (26), otherwise, it can be roughly estimated following Wang and Morton (2021a) based on the partial TEC above the receiver orbit:

$$sTEC_D = \frac{(1-\beta) \cdot vTEC_{LEO}}{m(\alpha)} \tag{28}$$

$$m(\alpha) = \frac{\sin\alpha + \sqrt{(\frac{R_{shell}}{R_{orbit}})^2 - (\cos\alpha)^2}}{1 + R_{shell}/R_{orbit}} \tag{29}$$

where $1-\beta$ represents the proportion of vertical TEC above the LEO orbit at the receiver location, $m(\alpha)$ is a "geometric" mapping function (Foelsche and Kirchengast, 2002) calculated based on the elevation angle α from receiver to GNSS satellite (as labeled in Fig. 2), and R_{shell} and R_{orbit}, which are the ionosphere thin shell and CubeSat orbit radii, respectively.

4.3. Troposphere

The tropospheric delay is a significant error source in GNSS-R phase altimetry, especially at low elevation angles. It can typically be modeled as two components: the hydrostatic (dry) component, which is caused by the dry gases in the atmosphere and is relatively stable and predictable, and the wet component, which is due to water vapor and is more variable and challenging to model accurately.

In this paper, the Vienna Mapping Functions 3 (VMF3) and the 1°×1° grid-wise ray-traced zenith delays product (Landskron and Böhm, 2018) are used to model the reflected signal tropospheric delay:

$$\hat{T}_R = 2 \cdot [ZHD \cdot m_{dry}(\theta) + ZWD \cdot m_{wet}(\theta)] \tag{30}$$

where m_{dry} and m_{wet} are the mapping functions in VMF3 for the zenith hydrostatic delay (ZHD) and zenith wet delay (ZWD), respectively. The grid data of zenith delays are generated every 6 h using ray tracing and meteorological data from European Centre for Medium-Range Weather Forecasts (ECMWF). The zenith delay error is primarily from the wet component due to the highly variable atmospheric water vapor.

The residual tropospheric delay-induced surface height error $\delta\tilde{H}_T$ is dependent on δZWD, θ, and their variations over the river-reflection segment. It can be modeled and analyzed based on Eqs. (8), (30) as:

$$\delta\tilde{H}_T = \frac{\delta ZWD \cdot m(\theta) - \overline{\delta ZWD \cdot m(\theta)}}{2 \cdot \sin(\theta)} \tag{31}$$

where $\bar{}$ denotes the mean value of the variables under it, and δZWD is the error in VMF3 ZWD. A significant river slope error arises from the δZWD gradient or variation at low elevation angle, and for simplicity, it is approximated to be:

$$\delta\dot{H}_T = \frac{\delta\dot{ZWD}}{2 \cdot \sin^2(\theta)} \tag{32}$$

where $\delta\dot{ZWD}$ is the gradient of δZWD. The approximation of the mapping function with $1/\sin(\theta)$ introduces minor uncertainty in the analysis, e.g., for track #c1 at a relatively low elevation angle of 12°, the difference between the VMF3 mapping function and $1/\sin(\theta)$ approximation is only about 1%. The ZWD gradient $\dot{ZWD}$ is typically a small fraction of 1 mm/km, and it can exceed 1 mm/km and even reach up to several mm/km in extreme weather conditions. For instance, $\delta\dot{ZWD}$ = 1 mm/km leads to river slope retrieval errors of 0.74, 0.20, and 0.10 cm/km for reflection signal elevation angles at 15°, 30°, and 45°, respectively. The VMF3 ZWD bias (its mean value over the segment) also contributes to the river slope retrieval error due to variations in the elevation angle over a reflection track. However, it is typically less significant compared to the ZWD error gradient.

4.4. Carrier phase noise

Phase noise is a critical factor affecting the precision of GNSS-R phase altimetry and the accuracy of river slope measurements. It originates from various sources, such as the thermal noise within the receiver electronic components, receiver oscillators, analog-to-digital conversions, etc., and depends on the signal-to-noise ratio. Multipath effects are also considered here as noise. To estimate the standard deviation (std) of phase noise, all cycle slips are first corrected, and clear

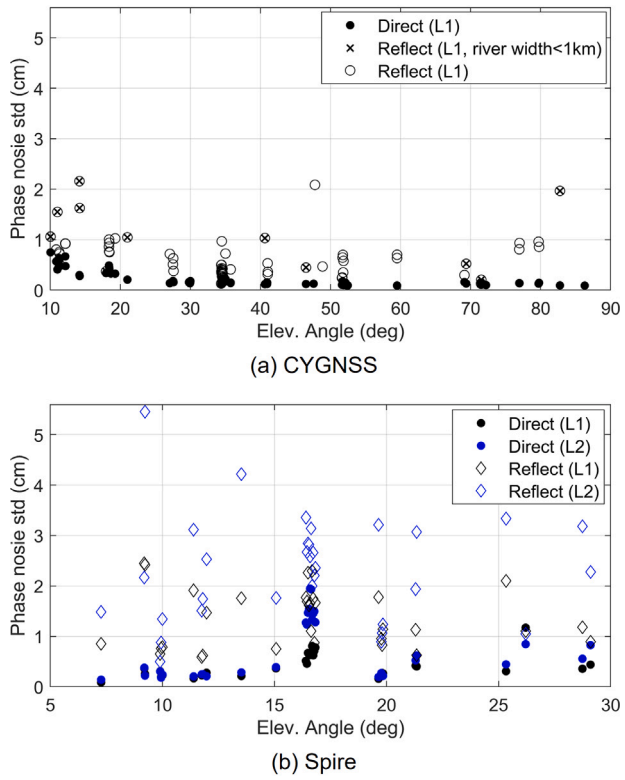


Fig. 5. Phase noise standard deviations estimated for selected 1-s segments of direct signals and reflected signals over river surfaces from (a) CYGNSS raw IF data processed by OL tracking using 10-ms coherent integration and (b) Spire grazing-angle GNSS-R data from OL tracking using 20-ms coherent integration.

outliers are removed. Then, a third-order polynomial trend is fitted and removed for each one-second (or shorter) segment of phase samples. Finally, the standard deviation of the residual phase is calculated.

Fig. 5 depicts the standard deviations of phase noise for both direct and river-reflected GNSS signals, comparing CYGNSS raw IF data and Spire grazing-angle GNSS-R data. The phase noise standard deviations are determined for each manually selected river-reflected segment, ensuring that the SP is at least 200 m away from the riverbank. The analysis is based on 32 segments of reflected signal from CYGNSS raw IF data and 17 segments from Spire data, including those listed in Table 1 and additional segments to span the range of elevation angles. Here two primary factors that impact the phase noise are considered : SNR and the presence of multipath interference. SNR depends on the antenna gain pattern, which varies with elevation angles. Moreover, multipath interference in the reflected signal can also be significantly affected by elevation angles, particularly in the case of narrow rivers. Lower elevation angles result in a larger reflection footprint, increasing the likelihood of multipath signals reflecting off land and causing interference. Consequently, the standard deviations of phase noise are plotted against elevation angles to depict these dependencies, and reflections over narrow river sections are separately highlighted for the CYGNSS raw IF measurements. It is also noteworthy, as shown in Table 1, that most reflection tracks from Spire data are associated with river widths of approximately 1 km or narrower, with the exception of track s16.

For direct signals, the mean phase noise standard deviations are 0.21 cm, 0.42 cm, and 0.71 cm for CYGNSS raw IF (at L1 frequency), Spire L1, and Spire L2 data, respectively. The phase noise standard deviation decreases with elevation angle for CYGNSS data, whereas it shows an inverse relationship for Spire data. This trend aligns with their respective antenna gain patterns: CYGNSS GNSS-R antennas are oriented towards an off-nadir angle of 28° degrees, while Spire CubeSats' RO antennas face the Earth limb.

The reflected signals are noisier compared to the direct signals, with mean phase noise standard deviations of 0.85 cm for the selected CYGNSS data (0.98 cm for those reflected over narrow river sections with width < 1 km), 1.69 cm for Spire L1 measurements, and 2.82 cm for Spire L2 measurements. The CYGNSS phase measurements are overall more precise than Spire data, and this is likely because of the higher antenna gain and LHCP. Additionally, larger phase noise standard deviations are observed in CYGNSS measurements at elevation angles below 20° or above 70°. At lower elevation angles, the increased phase noise may result from reduced antenna gain and multipath interference, while at higher elevation angles, it is likely attributed to reflection coherence. The river surface roughness may impact the reflection coherence, particularly at high elevation angles, leading to low specularly reflected signal energy and large noise the carrier phase measurement. In contrast, reflected phase noise from Spire data appears relatively consistent across elevation angles ranging from approximately 7° to 30°.

Assuming an ideal river section, where the river slope estimation becomes a linear regression problem using the GNSS-R retrieved relative heights, the slope standard deviation due to phase noise can be approximated by the two equations below for single-frequency (CYGNSS) and dual-frequency (Spire) measurements, respectively.

$$\sigma_{\mathrm{S,single}} = \frac{\sqrt{\sigma_{\mathrm{D}}^2 + \sigma_{\mathrm{R}}^2}}{\sqrt{\sum_{i=1}^{N}(x_i - \bar{x})^2}} \tag{33}$$

$$\sigma_{\mathrm{S,dual}} = \frac{\sqrt{\sigma_{\mathrm{D,iono\text{-}free}}^2 + \sigma_{\mathrm{R,iono\text{-}free}}^2}}{\sqrt{\sum_{i=1}^{N}(x_i - \bar{x})^2}} \tag{34}$$

where σ is the noise standard deviation, with subscripts S, D, R, and iono-free denoting river slope, direct signal phase, reflected signal phase, and ionospheric-free (iono-free) combination of phase, respectively, x is the distance between the SP and the start of the river-reflection segment, and N is the number of measurement samples. The noise standard deviation of the dual-frequency phase ionospheric-free combination can be derived from Eqs. (25), (26), for example, for the direct signal:

$$\sigma_{\mathrm{D,iono\text{-}free}} = \sqrt{\left(\frac{f_1^2}{f_1^2 - f_2^2}\right)^2 \sigma_{\mathrm{D},1}^2 + \left(\frac{f_2^2}{f_1^2 - f_2^2}\right)^2 \sigma_{\mathrm{D},2}^2} \tag{35}$$

where additional subscripts 1 and 2 denote GNSS signals at frequencies $f1$ and $f2$, respectively. The ionospheric-free combination standard deviation $\sigma_{\mathrm{R,iono\text{-}free}}$ can be calculated similarly for the reflected signal.

As shown in Eqs. (33), (34), the error in GNSS-R measurement of river slope also depends on the length of the river-reflection segment and the number of phase samples N. The noise-induced error diminishes with a longer data segment and a higher number of data samples. Spire GNSS-R data is provided at a fixed rate of 50 Hz. In this study, the CYGNSS raw IF data is processed with 10-ms coherent integration, yielding 100-Hz phase data samples.

Fig. 6 shows the standard deviations of noise-induced river slope error, calculated using the measurement data rates, the previously discussed mean phase noise standard deviations for CYGNSS and Spire data, and an assumption that the SP moves at 5 km/s. This analysis shows that the phase noise performance, as determined by the receiver hardware (such as antenna gain and polarization, clock, sampler and digitizer, etc.) may result in a ~2.4 times greater standard deviation in river slope measurement from Spire data compared to CYGNSS raw IF data (both using single-frequency carrier phase measurements and model-based ionospheric correction). Moreover, the dual-frequency ionospheric correction amplifies phase noise-induced river slope error by a factor of 3.6 compared to using single-frequency

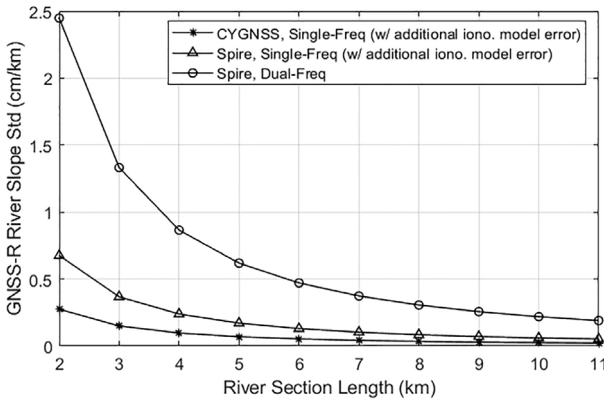


Fig. 6. Standard deviations of phase noise-induced error in GNSS-R river slope measurement at 30° elevation angle, as a function of the length of the river-reflection segment, for both CYGNSS (100-Hz single-frequency phase estimated from OL tracking of raw IF data) and Spire measurements.

(L1) phase only for Spire data. Therefore, ionospheric correction using dual-frequency phase is not always more advantageous than using ionospheric TEC products, particularly for short river-reflection segments and under quiet ionosphere conditions, as also noted in Wang and Morton (2022b).

4.5. Error budget summary

Table 2 summarizes the primary error terms affecting GNSS-R river slope measurements as discussed above, including residual errors from satellite orbits, reference surface heights, tropospheric delay, ionospheric effects, phase noise, and the total error in river slope measurements. The magnitudes for each error term and the total error are estimated approximately as the standard deviations of their corresponding river slope errors, based on the statistics of elevation angles and phase noise of CYGNSS raw IF and Spire GNSS-R data and a few other assumptions.

For the analysis of residual error from tropospheric delay after applying the VMF3 correction, we assumed a standard deviations of 1 mm/km for the VMF3 ZTD error gradients, reflecting a moist and highly variable environment without extreme conditions. To streamline our analysis, a representative elevation angle of 30° is adopted for both CYGNSS raw IF and Spire GNSS-R data. The residual tropospheric delay contributes to river slope errors with standard deviations of approximately 0.2 cm/km. As the Spire data used in this study generally have lower elevation angles, 15° is analyzed as another representative elevation angle, where the residual tropospheric delay contributes to a 0.74 cm/km standard deviation in river slope measurement.

The residual ionospheric error in the Spire river slope measurement is negligible, after the correction using dual-frequency carrier phase. In contrast, for CYGNSS measurements utilizing single-frequency carrier phase, the residual ionospheric error can exhibit considerable variability. For example, the ionospheric TEC gradients can remain minimal for short river-reflection segments, such as during local nighttime and in most mid-latitude regions. However, under disturbed ionospheric conditions, particularly when signals propagate through plasma structures, these TEC gradients can exceed (for example) 5 cm/km, and these gradients at such small scales (~10 km) can hardly be captured by global TEC maps. One such example is presented by Wang and Morton (2021a) (in Fig. 12).

However, the dual-frequency ionospheric correction amplifies the impact of phase noise by a factor of 3.6 in the retrieval of river slope. As a result, there are greater errors in river slope measurement from Spire data compared to CYGNSS data that are corresponding to phase noise. This difference is also attributed to higher phase noise and lower data rate in Spire data, stemming from hardware and software design constraints. Here, the phase-noise induced error is quantified over a 5-km track along an ideal river: the standard deviations of river slope are 0.10 cm/km for CYGNSS raw IF data and 0.60 cm/km for Spire data (using dual-frequency measurements for ionospheric correction) at 30° elevation angle, based on the phase noise standard deviations estimated for datasets in Table 1.

Therefore, for a 5-km GNSS-R track, the total standard deviations of river slope measurement error amount to 0.38 cm/km plus an additional ionospheric error for CYGNSS raw IF data, and 0.69 cm/km for Spire GNSS-R data, both at 30° elevation angle. The projection of phase-based range error to river slope error depends on the elevation angle θ by a factor of $1/2\sin(\theta)$, as in Eq. (8). Therefore, the accuracy of GNSS-R river slope measurement generally degrades with lower elevation angles. For example, the total root-sum-square (RSS) error of river slope measurement degrades to 1.50 cm/km for Spire data at 15°. This error quantification is based on the characterization of reflection geometry and phase noise from the selected datasets. It assumes ideal river conditions and does not account for factors such as ocean tidal effects, river superelevation, or measurement outliers due to multipath signals or land reflections.

Table 2
Estimated error contributions from major individual terms in GNSS-R river slope measurement at 30° elevation angle.

Error term	Slope error std (CYGNSS)	Slope error std (Spire)	Comment
Satellite orbits	0.2 cm/km	0.01 cm/km	–
Specular Point	0.24 cm/km (elev. angle 30°)	0.24 cm/km (elev. angle 30°)	Assuming std of 1 m for the reference surface height error
Troposphere	0.20 cm/km (elev. angle 30°)	0.20 cm/km (elev. angle 30°)	Assuming a moist environment with ZTD error gradient Std of 1 mm/km
Ionosphere	Variable*	Negligible	*varies with local time and ionospheric disturbance status: from minimal to exceeding 5 cm/km
Phase noise	0.07 cm/km	0.62 cm/km	Assuming a 5-km reflection segment over 1-km wide ideal river
Total (Root-Sum-Square)	0.38 cm/km + ionosphere model error	0.69 cm/km	Approximate std of river slope errors at 30° elev. angle

5. Results and validations

This section presents the outcomes of spaceborne GNSS-R river slope retrieval using CYGNSS raw IF and Spire datasets as listed in Table 1. The results are summarized in Fig. 7, evaluated based on the geoid model in flat water areas, and compared with gauge and satellite altimetry measurements, as detailed in the following subsections.

Fig. 7(a) and (b) depict maps of the Amazon River and lower Mississippi River regions. These maps showcase SP tracks from CYGNSS raw IF data (yellow) and Spire GNSS-R data (red), along with gauge stations (blue) and Hydroweb virtual stations (pink) that provide water level measurements. The river slopes estimated for each GNSS-R dataset are also highlighted. The GNSS-R measured river slopes in this paper are calculated along the river centerlines, instead of the SP tracks, assuming uniform water elevation across the river. Fig. 7(c) illustrates the calculation of river slope for track c14, over a wide and curved section of the Amazon River. Here, the slope is determined as the height

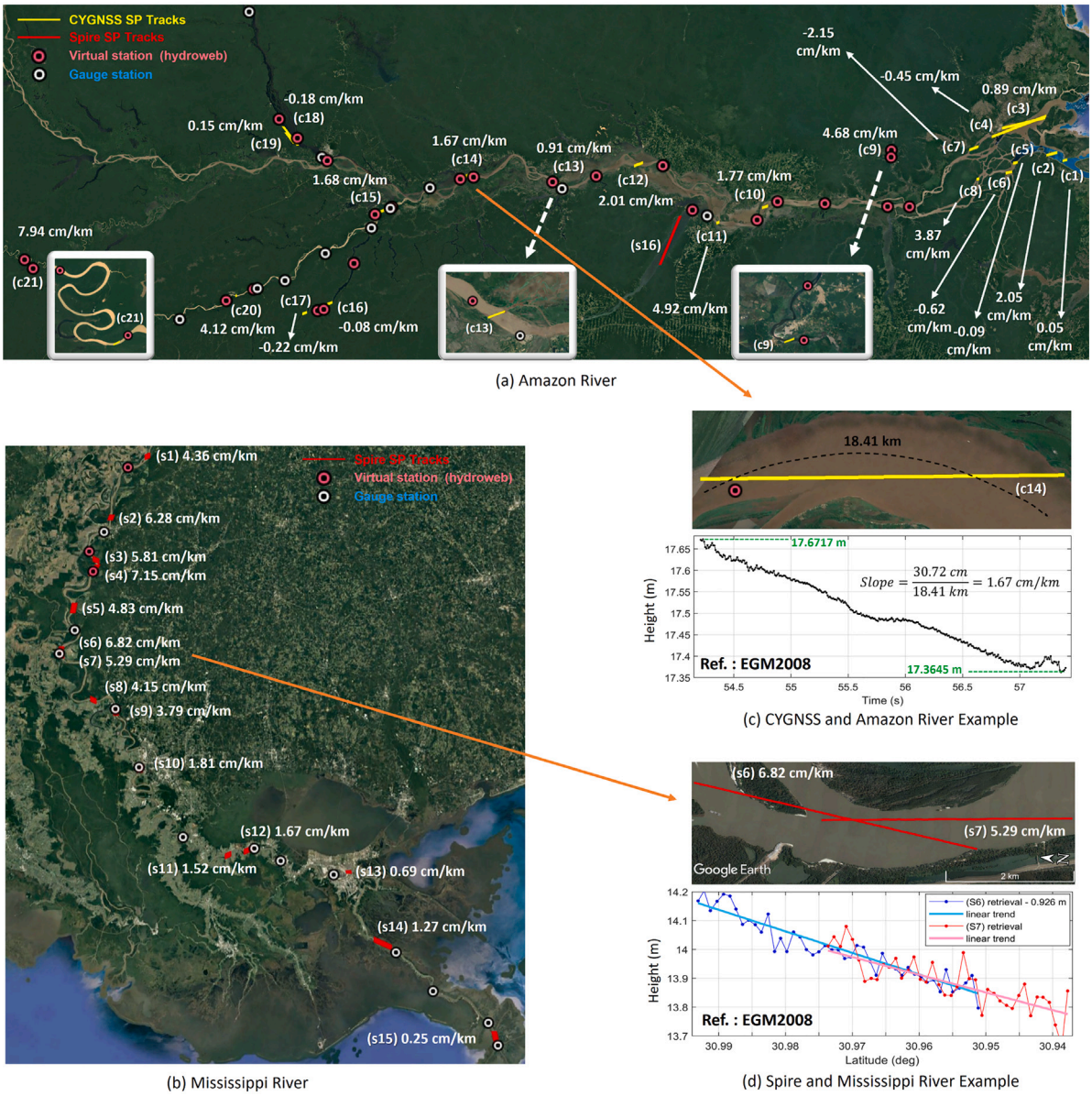


Fig. 7. Spaceborne GNSS-R tracks, river slope measurements, and nearby gauge and Hydroweb virtual stations in the Amazon River and Mississippi River areas for the selected data segments listed in Table 1. (a) shows the Amazon River and its tributaries, along with the SP tracks and river slope measurements from CYGNSS tracks c1–c21 and Spire track s16. (b) shows the lower Mississippi River, SP tracks, and river slope measurements from Spire tracks s1-s15. (c) shows the relative water level retrieved from CYGNSS track c14 and illustrates how the river slope is calculated. Specifically, for relatively long tracks, the slope is determined by the change in height over the length along the curved river centerline. (d) shows the relative water level retrieved from Spire tracks s6 and s7 (adjusted by 0.926 m to account for the absolute water level variation between two different dates and times). For shorter tracks, particularly those showing linear trends, river slopes are calculated based on linear regression. (For interpretation of the references to color in this figure legend, the reader is referred to the web version of this article.)

difference between the two ends of the SP track over the distance along the river centerline (visually identified using satellite images from Google Earth.). For shorter segments exhibiting linear trends, such as track s6 and s7 depicted in Fig. 7(d), height differences are determined from the estimated linear trends, and the slopes are still estimated along the river centerline. Overall, the GNSS-R river slope measurements exhibit reasonable magnitude. For instance, in Fig. 7(c) along the lower Mississippi River, the river slopes derived from Spire GNSS-R data demonstrate a noticeable decreasing trend along the flow direction and become quite gentle near the river mouth, e.g., 0.25 cm/km at track s15.

Validating each of these river slope measurements poses challenges, as discussed earlier in Section 1, due to the absence of existing data sources or remote sensing methods with sufficient precision to serve as ground truth. In this study, the GNSS-R-derived river slopes are compared against the geoid model (for flat water areas), as well as with gauge and satellite altimetry measurements, including data from the most recent SWOT mission. Details of these comparisons are discussed in the following subsections.

5.1. Flat water surfaces

The shape of lentic water surfaces (such as lakes and ponds) generally follows the geoid, which is the theoretical shape that the surface of the Earth would take under the influence of gravity and rotation alone, without any other forces acting upon it (like tides or winds). These areas with almost zero gradients (with respect to a geoid model such as EGM2008) can serve as "natural validation sites" for river slope measurements.

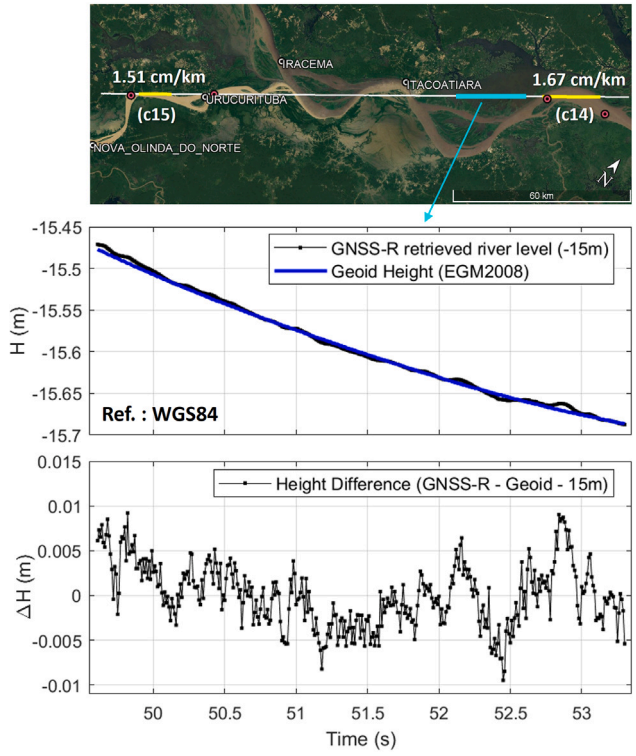


Fig. 8. Comparison of the GNSS-R retrieved relative water level and the EGM2008 geoid height: CYGNSS raw IF data of GPS signal reflected over Lake Lago Canacari. Top panel shows the lake-reflection SP track (bright blue), which is between the two river-reflection tracks c14 and c15, and all these three segments are from the same set of CYGNSS raw IF data and are of signals from the same GPS satellite. The satellite image is from an earlier date, potentially separated by months or years from the GNSS-R data. The middle panels show the EGM2008 geoid heights along the lake-reflection SP and the GNSS-R retrieved water surface heights (adjusted to have the same mean magnitudes with geoid height) with respect to the WGS84 ellipsoid. The bottom panel shows the height difference, i.e., the discrepancy between the GNSS-R retrieved relative water surface heights and the geoid model.

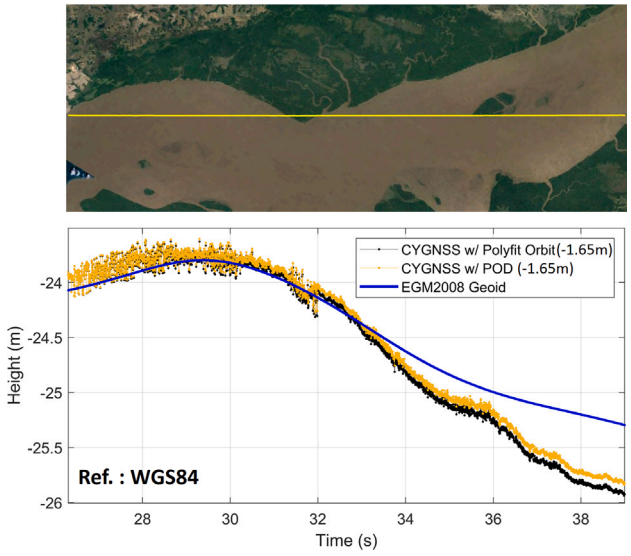


Fig. 9. Comparison of the GNSS-R retrieved relative water level and the EGM2008 geoid height for CYGNSS track c3. Two sets of GNSS-R water surface heights are retrieved using the polynomial orbit fit and precise orbit solution, respectively. Both results are adjusted by a constant value to align their magnitudes with the EGM2008 geoid height and are shown relative to the WGS84 ellipsoid in the bottom panel. The orbit error in the polynomial orbit fit results in a river slope error of 0.13 cm/km. The discrepancy between GNSS-R retrieved water surface height (yellow line) and the geoid model indicates a mean slope of 0.89 cm/km along the 76.8 km GNSS-R track. The satellite image is from an earlier date, potentially separated by months or years from the GNSS-R data. (For interpretation of the references to color in this figure legend, the reader is referred to the web version of this article.)

One such example is depicted in Fig. 8, where the top panel displays the SP tracks (shown in bright blue) over Lago Canacari, a lake situated adjacent to the Amazon River. Sentinel-2 images from a nearby date show a clear separation between this lake and the Amazon River. Therefore, we expect a flat water surface over the lake, making it suitable for GNSS-R validation. The reference surface height for this GNSS-R lake surface height retrieval is set to be 15 m relative to the EGM2008 geoid model, based on measurements from a Hydroweb virtual station. The middle panel displays the GNSS-R retrieved relative water surface heights, which are compared against the EGM2008 geoid model, with respect to the WGS84 ellipsoid. After adjusting their mean magnitudes to align with the EGM2008 geoid model, the relative water surface heights show perfect agreement. The bottom panel depicts the discrepancy between the GNSS-R relative water surface heights and the EGM2008 geoid, akin to the difference between the two lines in the middle panel. It highlights the sub-centimeter precision achievable by GNSS-R from space and underscores the high accuracy of GNSS-R phase-based relative altimetry, as evident from small slope errors in this instance.

The precision of these results aligns with and substantiate the error analysis discussed in Section 4 and Table 2 for CYGNSS raw IF data retrievals. This set of data was collected at 01:54 a.m. local time, during a period when the ionosphere is typically calm and thin, leading to small, negligible ionospheric TEC gradients. The high reflection angle of approximately 41° helps mitigate the tropospheric delay and ionospheric effects using models. The SP track spans approximately 30 km, which is sufficiently long to minimize phase noise impacts. This example underscores that GNSS-R river slope measurements using CYGNSS can achieve high accuracy, fractions of a centimeter per kilometer, particularly under conditions where the ionosphere exhibits gentle gradients. This lake reflection segment also validates the accuracy of nearby river slope measurements from tracks c14 and c15, as highlighted in the top panel. These two segments of data are from the same set of CYGNSS raw IF data and utilize the same GPS satellite signals, leading to a high level of confidence of their accuracy.

Another example is illustrated in Fig. 9 for CYGNSS track c3 over the Amazon River, near its mouth. The relative water surface heights are retrieved using the polynomial orbit fit and precise orbit solutions (as discussed in Section 3.3), respectively. Both results demonstrate good overall agreement with the EGM2008 geoid, and the comparison shows a 0.13 cm/km difference in river slope estimation, which is consistent with the quantified root mean square error of 0.2 cm/km as introduced by the simple polynomial fit of CYGNSS orbit.

Additionally, this example reveals features that help better understand GNSS-R performance and capabilities in relative altimetry and river slope measurement. The river water surface roughness has a significant impact on the phase noise magnitudes, as is evident in the segments before and after the 30-s mark. When the GNSS-R footprint overlaps with the land surface, it introduces biases in the retrieved relative heights, potentially causing them to decrease by several centimeters, as observed right before the 32-s mark. This occurs because the coherent signal energy is primarily from the water surface, and the equivalent SP of the water-reflected signal is displaced away from the center of the footprint.

This set of data was collected at 17:51 local time, when the ionosphere typically exhibits greater density and potentially larger TEC gradients compared to nighttime conditions. Apart from the residual ionospheric effects and the actual river surface gradients, the slight discrepancy observed in Fig. 9 may also be due to ocean tidal effects and potential errors in the EGM2008 geoid model, which is reported to have decimeter-level errors in South America (Blitzkow and Matos, 2009) due to the low density of terrestrial gravity measurements.

5.2. Comparison with gauge measurements

Water level gauges provide sub-centimeter accuracy in measurements with high temporal resolutions; however, their spatial distribution is sparse. The gauge stations used in this study are indicated in Fig. 7 and belong to the U.S. Geological Survey and the Brazilian Hydrometeorological Network maintained by Geological Survey of Brazil and Brazilian National Water Agency for the Mississippi River and Amazon River regions, respectively.

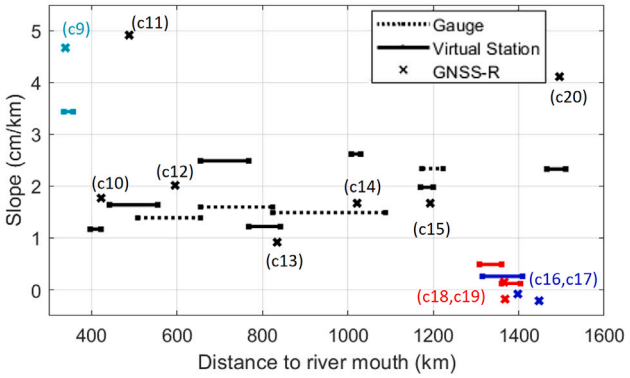
Fig. 10 compares the river slope measurements obtained from GNSS-R with the average river slope estimated between two nearby gauge stations, using gauge water levels recorded on the same day as the GNSS-R data. The results are plotted as a function of distance from the river mouth, with the average slopes estimated from gauge water levels represented as dashed lines and the GNSS-R measurements depicted as cross marks. Additionally, water level measurements from satellite altimetry at virtual gauge stations, as maintained by Hydroweb, are also included in this comparison, and the corresponding average river slopes between virtual stations are shown as solid lines. Different colors are used to distinguish measurements from different rivers or tributaries in the GNSS-R results plotted over distance from the river mouth. In Fig. 10(a) black cross marks denote GNSS-R measurements at the Madeira River and the main stream of the Amazon River; teal cross marks denote measurements at the Jari River; blue denotes measurements over the Conuma River; and red denotes measurements over the Negro River. In Fig. 10(b), black cross marks exclusively denote river slope measurements from Spire GNSS-R data over the main stream of the Mississippi River.

The GNSS-R retrieved river slope measurements generally exhibit good agreement with the average slopes between gauges or virtual stations. The majority of CYGNSS-derived measurements agree within approximately 0.5 cm/km, while the majority of Spire data-derived measurements agree within approximately 1 cm/km. The Spire measurements exhibit larger deviations from the average slopes between gauge/virtual stations compared to CYGNSS, however, the maximum absolute differences are still within approximately 2 cm/km. These results are consistent with the error analysis presented in Section 4 and Table 2, supporting the robust performance of GNSS-R for river slope retrieval under favorable conditions such as river width and track length.

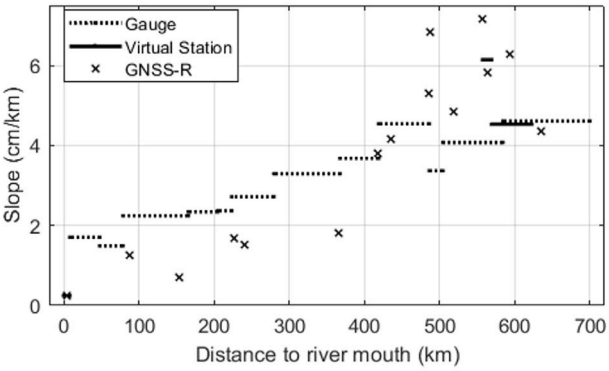
The comparison in Fig. 10 specifically includes CYGNSS tracks c9-c20; the absence of other tracks is due to data availability from gauge or virtual stations. Notably, larger discrepancies exceeding 1 cm/km are observed for tracks c9, c11, and c20. However, these discrepancies can be explained and do not necessarily indicate poor GNSS-R performance. Tracks c1–c9 are within 400 km from the river mouth and thus can experience significant tidal effects (Kosuth et al., 2009), which are not accounted for in this study. Track c11 traverses mostly across the river and intersects the riverbank at a curving point, where the larger slope is likely due to superelevation, and it can be used for calculating flow velocity. Track c20, being only 2.4 km long, may experience more significant phase noise impacts due to its shorter interval.

5.3. Comparison with in-situ measurements (from earlier years)

In-situ river slope measurements spatially overlapping with the presented CYGNSS observations in the Amazon region are available from field trips between 2008 and 2014. Despite being several years older than the CYGNSS data, these in-situ river slope measurements provide a valuable reference for evaluating the GNSS-R observations, as river slopes in the Amazon tend to remain stable over time. As shown in Fig. 11, the in-situ river WSE is measured by a GNSS receiver, supporting centimeter-level Precise Point Positioning (PPP), and a down-looking radar that measures the antenna height relative to the water surface. The river slope is calculated as the change in WSE divided by the distance along the river centerline.



(a) CYGNSS measurement of the Amazon River



(b) Spire measurement of the Mississippi River

Fig. 10. Comparison of GNSS-R measured river slopes (cross marks) and river slopes calculated between two gauge stations (dashed lines, recorded on the same day as GNSS-R) and/or Hydroweb virtual stations (solid lines, interpolated for the GNSS-R data recording date). The river slopes are calculated with respect to the EGM2008 geoid height. (a) shows river slope measurements from CYGNSS tracks c9-c20, different colors represent different tributaries of the Amazon River, and the absence of c1–c8 and c21 are due to unavailable gauge or virtual station water level measurements. (b) shows river slope measurements from Spire tracks s1-s15. (For interpretation of the references to color in this figure legend, the reader is referred to the web version of this article.)



Fig. 11. In-situ measurement of river slope.

In-situ river slope measurements coinciding with the GNSS-R data in both space and time are unavailable. Table 3 summarizes historical in-situ river slope measurements that correspond to a subset of the GNSS-R data and their respective dates. Fig. 12 compares these historical measurements with GNSS-R slope estimates derived from CYGNSS raw IF data. For tracks c10, c12, c14, c15, and c18, the GNSS-R slope retrievals align with the in-situ measurements (from different years) within approximately 0.5 cm/km. Track c20, with a length of only 2.4 km, shows better agreement between the GNSS-R slope retrieval and the in-situ measurements compared to gauge-derived river slopes (Fig. 10). The GNSS-R slope retrieval of Track c20 is 0.4–1.4 cm/km

Table 3
Summary of in-situ river slope measurements.

Track #	In-situ river slope (cm/km) [year-month]
C10	1.4 [2013-07]
C11	1.3 [2013-07]
C12	1.8 [2010-06], 2.6 [2013-03]
C13	2.5 [2013-03], 3.0 [2010-06]
C14	2.3 [2014-03], 2.1 [2013-03]
C15	1.8 [2013-09], 1.8 [2011-07], 1.3 [2009-12]
C18	0.3 [2008-06], 0.3 [2009-10]
C20	5.0 [2013-09], 5.5 [2013-09], 4.5 [2011-07], 5.0 [2009-12]

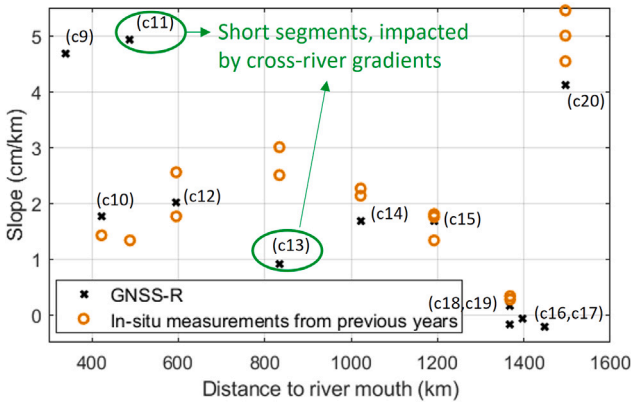


Fig. 12. Comparison of GNSS-R measured river slopes (cross marks) with available in-situ river slope measurements from earlier years.

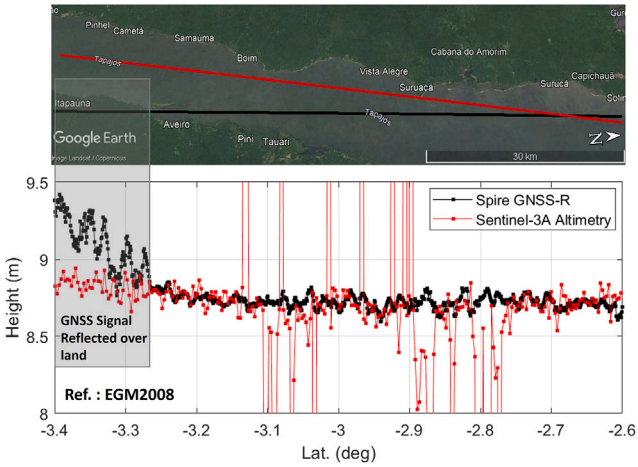


Fig. 13. Comparison of Spire GNSS-R relative water level retrieval from track s16 and Sentinel-3A altimetry data (on March 30, 2020) over the Tapajós River, a major tributary of the Amazon River. The Spire relative water level is adjusted to have the same mean magnitude as Sentinel altimetry data for the latitude range of −3.25° to −2.6° and filtered using a moving average with a window size of 20 samples. Sentinel-3 measurement has outliers out of the bound of the plot. The satellite image is from an earlier date, potentially separated by months or years from the GNSS-R data.

lower than the in-situ measurements, consistent with the uncertainty quantified for short segments in Fig. 6 and Table 2. Tracks c11 and c13 exhibit larger discrepancies from the in-situ measurements, likely due to the influence of cross-river gradients, as these tracks are oriented more across the river than along the river.

5.4. Comparison with satellite altimetry measurements

The relative river surface height measurements from GNSS-R are further compared with satellite altimetry measurements from Sentinel-3 and SWOT.

The relative water surface heights retrieved from Spire track s16 are compared with Sentinel-3A altimetry measurement in Fig. 13. The Sentinel-3A measurements are obtained from Level-2 land products (accessed through Copernicus Data Space Ecosystem). A moving average filter with a window size of 20 samples (0.4 s) is applied to the Spire relative height retrievals. Both measurements are displayed with respect to the EGM2008 geoid height. To align the Spire measurement of relative heights with the Sentinel-3A data within the latitude range of approximately −3.25° to −2.6°, a constant adjustment is applied to the Spire measurements. It should be noted that from −3.4° to −3.25° latitude, the GPS signal is reflected from land and does not offer meaningful measurement.

In general, the relative surface heights from Spire track s16 exhibit no discernible bias in their trends as compared to Sentinel-3A altimetry measurements, with both datasets indicating minimal slope of the Tapajos River. Furthermore, while Sentinel-3 data exhibits numerous measurement outliers, Spire data shows none, and both datasets demonstrate similar levels of noise.

Fig. 14 compares river surface height measurements from GNSS-R with SWOT at nearby locations but with a substantial time offset of approximately 3 years. The SWOT river heights are obtained from the SWOT Level 2 Water Mask Pixel Cloud Data Product, 'PIXC', PIC0 (Surface Water Ocean Topography (SWOT), 2024). For this comparison, the c12 CYGNSS SP Track over the Amazon River as well as the c15 CYGNSS SP Track over the Madeira River were selected. The PIXC pass (and tile) numbers that cover the two locations are 339(151) and 492(158) for c12 and 89(148) and 242(161) for c15. The SWOT data was downloaded using the earthaccess Python library. The data was then filtered such that only surface values equal to water near land and open water were selected, and all measurements flagged as bright land were removed. The geolocation quality flag was not applied as it appeared to mask valid measurements near c12. In addition to the flags, the PIXC data was filtered using a Sentinel-2 L2A Scene Classification map to remove all measurements classified as land (Modified Copernicus Sentinel data [2024]/Sentinel Hub), and a 3-sigma outlier detection of the detrended water surface height residuals. Although there are higher level SWOT data products (i.e. SWOT L2 HR RiverSP Node data product) that provide river slope and mean river height measurements from which slope can be estimated, the slope sensitivity to the sections of the river used to estimate slope results in too much variability to provide a detailed analysis. Directly comparing the high-level products would be suitable if GNSS-R could exactly match the sections of the river used to derive the slopes from the RiverSP product, which it cannot. Instead, the SWOT data are matched to GNSS-R, and to do this requires the high spatial resolution from the PIXC product.

The geolocation of each GNSS-R measurement in both c12 and c15 was mapped onto each overlapping PIXC pass and tile. The PIXC data were then matched to the GNSS-R tracks by taking the mean of all PIXC measurements within a 300 m radius of the footprint center for each GNSS-R sample, thus providing for each pass measurements of SWOT river height corresponding to each GNSS-R measurement. The footprint of the averaged SWOT measurement is close to the footprint size of the GNSS-R measurement at elevation angles higher than about 30°. Although the GNSS-R and SWOT measurements are separated by three years, they demonstrate good agreement in the measured water surface gradients. For track c12, discrepancies are observed over the initial 2 km, while the remaining approximately 12 km show good agreement between GNSS-R and SWOT. In the case of c15, GNSS-R measurements consistently align with SWOT data throughout the 12-km track and exhibit higher precision. The higher precision can lead to better river slope accuracy when estimated over shorter river sections, for example, over 5 km.

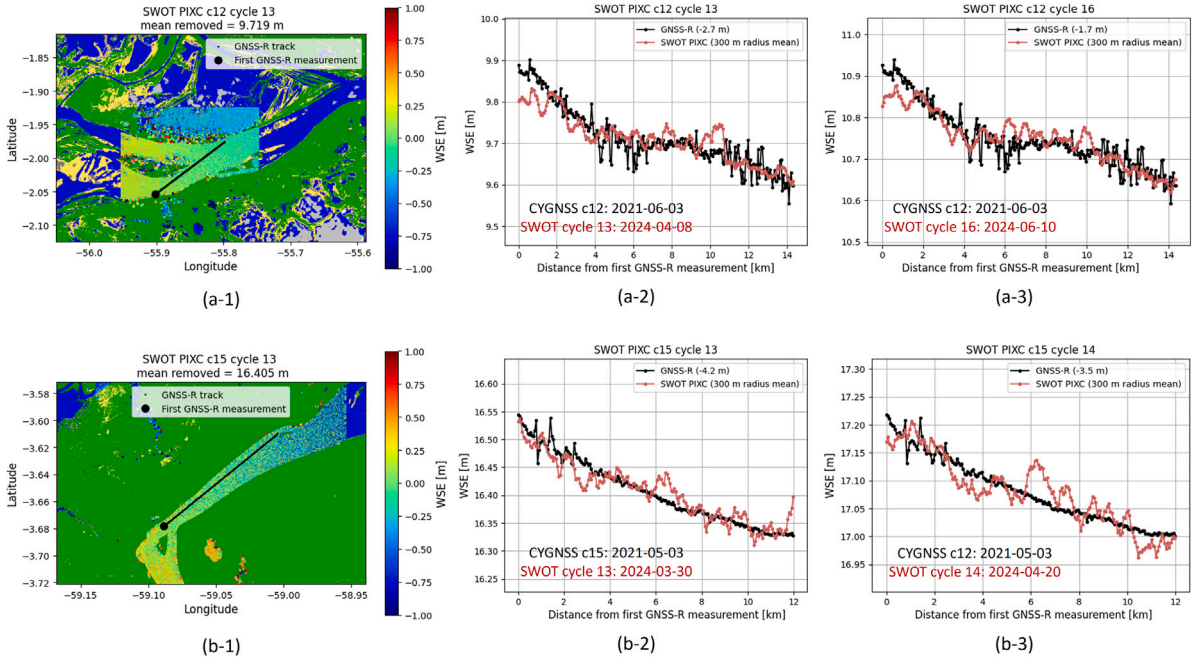


Fig. 14. Comparison of water surface elevation (WSE) measurements from GNSS-R (CYGNSS tracks c12 and c15) and SWOT. All WSEs are referenced to the EGM2008 geoid. The unfiltered relative WSEs estimated from GNSS-R carrier phase are adjusted by constant offsets to align with the SWOT measurements. The SWOT WSEs are derived from the pixel cloud (PIXC) data, averaged over a 300-m radius for each corresponding GNSS-R sample. Panel (a-1) shows the SWOT WSE measurement (with a mean value of 9.719 m removed) in the target area, with the black line representing the SP track of CYGNSS c12. The measurements have been overlaid on top of Sentinel-2 L2A Scene classification maps acquired as close as possible to the SWOT measurement date with cloud coverage less than 5% (2024-02-23 for c12 and 2024-02-21 for c15). Panels (a-2) and (a-3) compare the WSEs between CYGNSS c12 and SWOT cycles 13 and 16, respectively. Panels (b-1) to (b-3) present the same layout for CYGNSS track c15 and its comparisons with SWOT cycles 13 and 14.

The comparisons underscore the accuracy and precision of river water surface gradient measurements obtained from GNSS-R, demonstrating their ability to complement SWOT and other existing river monitoring systems.

6. Conclusion

This study aims to demonstrate that spaceborne GNSS-R is a viable method for observing river slopes. The coherent reflection measurement in spaceborne GNSS-R has a spatial resolution ranging from a few hundred meters to a few kilometers, depending on the reflection geometry. In this paper, this technique is demonstrated to be applicable to river sections wider than approximately 500 m, where the GNSS signal is reflected over the river surface for at least a few kilometers. Analysis of the error budget indicates an accuracy of fractions of 1 cm/km at elevation angles of about 30°, based on the characterization of both CYGNSS raw IF and Spire grazing-angle GNSS-R data measurements. The accuracy degrades with lower elevations angles, and it also can be further improved by measuring at higher elevation angles and upgrading the antenna and receiver hardware to reduce phase noise. This accuracy is higher than that of most other remote sensing approaches for measuring river slope. Furthermore, the relatively low cost, small size, and low power consumption of GNSS-R receivers offer the potential for obtaining river slope measurements with dense spatial coverage and short revisit times and to complement existing river observation systems. This paper has addressed this technique in three main aspects: methodologies applied to data from existing GNSS-R systems, error analysis and quantification, and performance validation, which are summarized as follows.

Currently, there are no operational missions specifically designed for GNSS-R altimetry applications, although the upcoming HydroGNSS mission is expected to incorporate dedicated coherent channels to enable carrier phase measurements. In this study, we demonstrate GNSS-R measurement of river slope using both CYGNSS raw IF data and Spire grazing-angle GNSS-R data. Each data source has its limitations for this application. CYGNSS, in its standard operation, does not support phase measurements and lacks the dual-frequency capability necessary for ionospheric correction. Spire grazing-angle GNSS-R data provides dual-frequency measurements but is limited to grazing-angle reflections, and it has in general higher phase noise compared to measurements obtained from CYGNSS raw IF data. Combining these two data sources helps us establish a realistic expectation of achievable accuracy in future missions. Additionally, we develop a comprehensive data processing workflow for CYGNSS raw IF data, encompassing the entire process from raw IF samples to the calculation of river slopes. The methodologies are detailed in Section 3 and are demonstrated to be effective in producing accurate river slope measurements.

The accuracy of river slope measurements using GNSS-R is analyzed and discussed in Section 4. Major error factors considered in this study include satellite orbits, specular point estimation, tropospheric delay, ionospheric effects, and phase noise. Root mean square errors for each factor are quantified for measurements using CYGNSS raw IF data and Spire grazing-angle GNSS-R data, respectively. The total RSS error in river slope measurement is 0.38 cm/km plus ionosphere TEC model error for CYGNSS and 0.69 cm/km for Spire with dual-frequency ionospheric correction at 30° elevation angle. Dual-frequency ionospheric correction is necessary under active ionosphere conditions, although it amplifies the error from phase noise. To simplify the data processing, a polynomial fit for the CYGNSS orbit is adopted in this study, instead of running the Gipsy software to obtain precise orbit solutions for all datasets. The orbit gradient error associated with the polynomial orbit fit is counted in the error analysis leading to a total error of 0.38 cm/km for CYGNSS, which can be further improved to 0.36 cm/km by employing POD, at the same elevation angle of 30°. Degraded accuracy is expected at lower elevation angles, for example, 1.50 cm/km for using Spire data at 15° elevation angle. These quantified errors are validated in Section 5, where examples over known flat water areas are discussed and all GNSS-R river slope measurements are compared

against measurements from nearby gauges, Hydroweb virtual stations, Sentinel-3, and SWOT. These analyses and comparisons consistently demonstrate the high accuracy and precision of GNSS-R in measuring river slopes.

This paper presents the methodologies and an assessment of GNSS-R performance and capability in measuring river slopes. The assessment is based on 21 river-reflection segments selected from CYGNSS raw IF data and 16 segments from Spire grazing-angle GNSS-R. A critical criterion for selecting these segments is that reflections occur at least 200 m away from river banks. Further studies are necessary to develop methods to quantify the uncertainty for individual measurements and to explore the boundaries of this technique, for instance, the minimum river width and/or distance from riverbanks required for reliable GNSS-R measurements. The GNSS-R river slope accuracy can be enhanced by incorporating SWOT data to model the reflection geometry. For river sections with steeper gradients (exceeding those studied here), the reflection geometry should be further modeled and analyzed based on a reference river slope, and the associated uncertainties should be thoroughly evaluated and validated. Additionally, there is a need to develop a robust method and specific criteria for automatically identifying useful data segments to calculate river slopes. These efforts are essential for achieving a comprehensive characterization of the temporal and spatial sampling capabilities and accuracy of spaceborne GNSS-R in river surface monitoring.

CRediT authorship contribution statement

Yang Wang: Writing – review & editing, Writing – original draft, Visualization, Validation, Methodology, Funding acquisition, Formal analysis, Conceptualization. **Y. Jade Morton:** Writing – review & editing, Funding acquisition, Conceptualization. **J. Toby Minear:** Writing – review & editing, Validation, Conceptualization. **Alexa Putnam:** Writing – review & editing, Visualization, Validation. **Alex Conrad:** Writing – review & editing, Methodology. **Penina Axelrad:** Writing – review & editing, Methodology. **R. Steven Nerem:** Writing – review & editing. **April Warnock:** Writing – review & editing. **Christopher Ruf:** Writing – review & editing. **Daniel Medeiros Moreira:** Writing – review & editing, Validation. **Matthieu Talpe:** Writing – review & editing.

Declaration of competing interest

The authors declare that they have no known competing financial interests or personal relationships that could have appeared to influence the work reported in this paper.

Acknowledgments

This study is supported by NASA grants 80NSSC21K1011, 80NSSC22K1116, and 80NSSC23K1056. The Spire grazing-angle GNSS-R data utilized in this work was made available through the NASA Commercial Smallsat Data Acquisition (CSDA) Program. We would like to thank Dr. M. Yu for creating Fig. 1.

Data availability

The CYGNSS raw IF data is available at NASA PO.DAAC: https://podaac.jpl.nasa.gov/dataset/CYGNSS_L1_RAW_IF. The Spire grazing-angle GNSS-R data is accessible through the Smallsat Data Explorer (available to U.S. Government-funded researchers): https://www.earthdata.nasa.gov/esds/csda/smallsat-data-explorer. The SWOT data is available at NASA PO.DAAC: https://podaac.jpl.nasa.gov/SWOT. The Sentinel data is accessed through the CREODIAS Data Explorer: https://explore.creodias.eu/. The VMF3 data and tools are available from the VMFDataServer re3data.org (2021). The ionospheric TEC data from the Madrigal Database is available at: http://cedar.openmadrigal.org. Water data from gauges is accessed through: https://waterdata.usgs.gov/nwis and https://www.snirh.gov.br/hidroweb/serieshistoricas. Water data from Hydroweb was accessed through: https://www.theia-land.fr/en/hydroweb and is now moved to https://www.theia-land.fr/en/typeofproduct/hydroweb-nexten/.

References

Al-Khaldi, M.M., Johnson, J.T., Gleason, S., Chew, C.C., Gerlein-Safdi, C., Shah, R., Zuffada, C., 2021. Inland water body mapping using CYGNSS coherence detection. IEEE Trans. Geosci. Remote Sens. 59 (9), 7385–7394.

Al-Khaldi, M.M., Johnson, J.T., O'Brien, A.J., Balenzano, A., Mattia, F., 2019. Time-series retrieval of soil moisture using CYGNSS. IEEE Trans. Geosci. Remote Sens. 57 (7), 4322–4331.

Alonso-Arroyo, A., Zavorotny, V.U., Camps, A., 2017. Sea ice detection using UK TDS-1 GNSS-R data. IEEE Trans. Geosci. Remote Sens. 55 (9), 4989–5001.

Alsdorf, D.E., Rodríguez, E., Lettenmaier, D.P., 2007. Measuring surface water from space. Rev. Geophys. 45 (2).

Altenau, E.H., Pavelsky, T.M., Durand, M.T., Yang, X., Frasson, R.P.d.M., Bendezu, L., 2021. The Surface Water and Ocean Topography (SWOT) Mission River Database (SWORD): A global river network for satellite data products. Water Resour. Res. 57 (7), e2021WR030054.

Bertiger, W., Bar-Sever, Y., Dorsey, A., Haines, B., Harvey, N., Hemberger, D., Heflin, M., Lu, W., Miller, M., Moore, A.W., et al., 2020. GipsyX/RTGx, a new tool set for space geodetic operations and research. Adv. Space Res. 66 (3), 469–489.

Bilitza, D., 2018. International Reference Ionosphere 2016: From ionospheric climate to real-time weather predictions. Space Weather 16 (11), 1804–1810.

Blitzkow, D., Matos, A., 2009. EGM2008 and PGM2007A evaluation for South America. Newton's Bull. 4, 79–89.

Brazilian National Water Agency, 2024. Brazilian hydrometeorological network data. accessed [20 July 2024], at URL [https://www.snirh.gov.br/hidroweb/serieshistoricas/].

Bruinsma, S., Thuillier, G., Barlier, F., 2003. The DTM-2000 empirical thermosphere model with new data assimilation and constraints at lower boundary: accuracy and properties. J. Atmos. Sol.-Terr. Phys. 65 (9), 1053–1070.

Camps, A., 2019. Spatial resolution in GNSS-R under coherent scattering. IEEE Geosci. Remote Sens. Lett. 17 (1), 32–36.

Cardellach, E., Li, W., Rius, A., Semmling, M., Wickert, J., Zus, F., Ruf, C.S., Buontempo, C., 2019. First precise spaceborne sea surface altimetry with GNSS reflected signals. IEEE J. Sel. Top. Appl. Earth Obs. Remote Sens. 13, 102–112.

Carreno-Luengo, H., Ruf, C.S., 2021. Retrieving freeze/thaw surface state from CYGNSS measurements. IEEE Trans. Geosci. Remote Sens. 60, 1–13.

Cartwright, J., Talpe, M., Nguyen, V., Jales, P., Nogues-Correig, O., Yuasa, T., Irisov, V., Masters, D., 2021. Sea ice remote sensing by the spire EO constellation. In: AGU Fall Meeting Abstracts. Vol. 2021, pp. C32C–08.

Chew, C.C., Shah, R., Zuffada, C., Mannucci, A.J., 2016. Wetland mapping and measurement of flood inundated area using ground-reflected GNSS signals in a bistatic radar system. In: 2016 IEEE International Geoscience and Remote Sensing Symposium. IGARSS, IEEE, pp. 7184–7187.

Chew, C., Small, E., 2018. Soil moisture sensing using spaceborne GNSS reflections: Comparison of CYGNSS reflectivity to SMAP soil moisture. Geophys. Res. Lett. 45 (9), 4049–4057.

Clarizia, M.P., Ruf, C., Cipollini, P., Zuffada, C., 2016. First spaceborne observation of sea surface height using GPS-Reflectometry. Geophys. Res. Lett. 43 (2), 767–774.

Conrad, A.V., Axelrad, P., Haines, B., Zuffada, C., O'brien, A., 2023. Improved GPS-based single-frequency orbit determination for the CYGNSS spacecraft using GipsyX. Navig.: J. Inst. Navig. 70 (1).

Copernicus Data Space Ecosystem, 2024. Sentinel-3 data. accessed [08 December 2024], at URL [https://dataspace.copernicus.eu/].

CYGNSS raw IF, 2020. CYGNSS level 1 raw intermediate frequency data record. http://dx.doi.org/10.5067/CYGNS-L1RIF, URL https://podaac.jpl.nasa.gov/dataset/CYGNSS_L1_RAW_IF.

Da Silva, J.S., Calmant, S., Seyler, F., Rotunno Filho, O.C., Cochonneau, G., Mansur, W.J., 2010. Water levels in the Amazon basin derived from the ERS 2 and ENVISAT radar altimetry missions. Remote Sens. Environ. 114 (10), 2160–2181.

Egido, A., Paloscia, S., Motte, E., Guerriero, L., Pierdicca, N., Caparrini, M., Santi, E., Fontanelli, G., Floury, N., 2014. Airborne GNSS-R polarimetric measurements for soil moisture and above-ground biomass estimation. IEEE J. Sel. Top. Appl. Earth Obs. Remote Sens. 7 (5), 1522–1532.

Esteban Fernandez, D., Pollard, B., Vaze, P., Abelson, R., 2017. SWOT Project Mission Performance and Error Budget. Jet Propulsion Laboratory Document D-79084 Revision A.

Farr, T.G., Rosen, P.A., Caro, E., Crippen, R., Duren, R., Hensley, S., Kobrick, M., Paller, M., Rodriguez, E., Roth, L., et al., 2007. The shuttle radar topography mission. Rev. Geophys. 45 (2).

Foelsche, U., Kirchengast, G., 2002. A simple "geometric" mapping function for the hydrostatic delay at radio frequencies and assessment of its performance. Geophys. Res. Lett. 29 (10), 111.
Foti, G., Gommenginger, C., Jales, P., Unwin, M., Shaw, A., Robertson, C., Rosello, J., 2015. Spaceborne GNSS reflectometry for ocean winds: First results from the UK TechDemoSat-1 mission. Geophys. Res. Lett. 42 (13), 5435–5441.
Garrison, J.L., Komjathy, A., Zavorotny, V.U., Katzberg, S.J., 2002. Wind speed measurement using forward scattered GPS signals. IEEE Trans. Geosci. Remote Sens. 40 (1), 50–65.
Gleason, S., 2006. Remote Sensing of Ocean, Ice and Land Surfaces Using Bistatically Scattered GNSS Signals from Low Earth Orbit (Ph.D. thesis). University of Surrey.
Gleason, S., 2010. Towards sea ice remote sensing with space detected GPS signals: Demonstration of technical feasibility and initial consistency check using low resolution sea ice information. Remote Sens. 2 (8), 2017–2039.
Hannah, D.M., Demuth, S., Lanen, H.v., Looser, U., Prudhomme, C., Rees, G., Stahl, K., Tallaksen, L.M., 2011. Large-scale river flow archives: importance, current status and future needs.
Heldmyer, A., Livneh, B., McCreight, J., Read, L., Kasprzyk, J., Minear, T., 2021. Evaluation of a new observationally based channel parameterization for the national water model. Hydrol. Earth Syst. Sci. Discuss. 2021, 1–27.
International GNSS Service, 2010. GNSS final combined orbit solution product, Greenbelt, MD, USA:NASA Crustal Dynamics Data Information System (CDDIS). http://dx.doi.org/10.5067/gnss/gnss_igsorb_001.
Jasinski, M., Stoll, J., Hancock, D., Robbins, J., Nattala, J., Morison, J., Jones, B., Ondrusek, M., Pavelsky, T., Parrish, C., 2021. Algorithm theoretical basis document (ATBD) for along track inland surface water data, release 004.
Julien, P.Y., 2018. River dynamics. In: River Mechanics. Cambridge University Press, pp. 292–329.
Katzberg, S.J., Torres, O., Grant, M.S., Masters, D., 2006. Utilizing calibrated GPS reflected signals to estimate soil reflectivity and dielectric constant: Results from SMEX02. Remote Sens. Environ. 100 (1), 17–28.
Kleinherenbrink, M., Naeije, M., Slobbe, C., Egido, A., Smith, W., 2020. The performance of CryoSat-2 fully-focussed SAR for inland water-level estimation. Remote Sens. Environ. 237, 111589.
Knocke, P., Ries, J., Tapley, B., 1988. Earth radiation pressure effects on satellites. In: Astrodynamics Conference. p. 4292.
Komjathy, A., Zavorotny, V.U., Axelrad, P., Born, G.H., Garrison, J.L., 2000. GPS signal scattering from sea surface: Wind speed retrieval using experimental data and theoretical model. Remote Sens. Environ. 73 (2), 162–174.
Kosuth, P., Callede, J., Laraque, A., Filizola, N., Guyot, J.L., Seyler, P., Fritsch, J.M., Guimaraes, V., 2009. Sea-tide effects on flows in the lower reaches of the Amazon River. Hydrol. Process.: Int. J. 23 (22), 3141–3150.
Landskron, D., Böhm, J., 2018. VMF3/GPT3: refined discrete and empirical troposphere mapping functions. J. Geod. 92, 349–360.
Li, W., Cardellach, E., Fabra, F., Ribo, S., Rius, A., 2018. Lake level and surface topography measured with spaceborne GNSS-reflectometry from CYGNSS mission: Example for the lake Qinghai. Geophys. Res. Lett. 45 (24), 13–332.
Li, W., Cardellach, E., Fabra, F., Ribó, S., Rius, A., 2019. Assessment of spaceborne GNSS-R ocean altimetry performance using CYGNSS mission raw data. IEEE Trans. Geosci. Remote Sens. 58 (1), 238–250.
Li, W., Cardellach, E., Fabra, F., Rius, A., Ribó, S., Martín-Neira, M., 2017. First spaceborne phase altimetry over sea ice using TechDemoSat-1 GNSS-R signals. Geophys. Res. Lett. 44 (16), 8369–8376.
Liu, Y., Collett, I., Morton, Y.J., 2019. Application of neural network to GNSS-R wind speed retrieval. IEEE Trans. Geosci. Remote Sens. 57 (12), 9756–9766.
Loria, E., O'brien, A., Zavorotny, V., Downs, B., Zuffada, C., 2020. Analysis of scattering characteristics from inland bodies of water observed by CYGNSS. Remote Sens. Environ. 245, 111825.
Martin-Neira, M., 1998. A passive reflectometry and interferometry system (PARIS): Application to ocean altimetry. ESA Spec. Publ. 2 (4), 479–482.
Martire, L., Runge, T.F., Meng, X., Krishnamoorthy, S., Vergados, P., Mannucci, A.J., Verkhoglyadova, O.P., Komjáthy, A., Moore, A.W., Meyer, R.F., et al., 2024. The JPL-GIM algorithm and products: multi-GNSS high-rate global mapping of total electron content. J. Geod. 98 (5), 1–25.
Mashburn, J., Axelrad, P., Lowe, S.T., Larson, K.M., 2018. Global ocean altimetry with GNSS reflections from TechDemoSat-1. IEEE Trans. Geosci. Remote Sens. 56 (7), 4088–4097.
Milani, A., Nobili, A.M., Farinella, P., 1987. Non-Gravitational Perturbations and Satellite Geodesy.
Montenbruck, O., 2003. Kinematic GPS positioning of LEO satellites using ionosphere-free single frequency measurements. Aerosp. Sci. Technol. 7 (5), 396–405.
Morris, M., Chew, C., Reager, J.T., Shah, R., Zuffada, C., 2019. A novel approach to monitoring wetland dynamics using CYGNSS: Everglades case study. Remote Sens. Environ. 233, 111417.
Morton, Y.T., van Graas, F., Zhou, Q., Herdtner, J., 2009. Assessment of the higher order ionosphere error on position solutions. Navigation 56 (3), 185–193.
Morton, Y.J., Yang, Z., Breitsch, B., Bourne, H., Rino, C., 2020. Ionospheric effects, monitoring, and mitigation techniques. In: Position, Navigation, and Timing Technologies in the 21st Century: Integrated Satellite Navigation, Sensor Systems, and Civil Applications. Vol. 1, Wiley Online Library, pp. 879–937.
Nguyen, V.A., Nogués-Correig, O., Yuasa, T., Masters, D., Irisov, V., 2020. Initial GNSS phase altimetry measurements from the spire satellite constellation. Geophys. Res. Lett. 47 (15), e2020GL088308.
OECD, 2016. Financial Management of Flood Risk. OECD Publishing, Paris, http://dx.doi.org/10.1787/9789264257689-en.
Pavlis, N.K., Holmes, S.A., Kenyon, S.C., Factor, J.K., 2012. The development and evaluation of the Earth Gravitational Model 2008 (EGM2008). J. Geophys. Res.: Solid Earth 117 (B4).
Paz, A.R., Collischonn, W., 2007. River reach length and slope estimates for large-scale hydrological models based on a relatively high-resolution digital elevation model. J. Hydrol. 343 (3–4), 127–139.
Pierdicca, N., Comite, D., Camps, A., Carreno-Luengo, H., Cenci, L., Clarizia, M.P., Costantini, F., Dente, L., Guerriero, L., Mollfulleda, A., et al., 2021. The potential of spaceborne GNSS reflectometry for soil moisture, biomass, and freeze–thaw monitoring: Summary of a European space agency-funded study. IEEE Geosci. Remote Sens. Mag. 10 (2), 8–38.
Pu, T., Gerlein-Safdi, C., Xiong, Y., Li, M., Kort, E.A., Bloom, A.A., 2024. Berkeley-RWAWC: a new CYGNSS-based watermask unveils unique observations of seasonal dynamics in the Tropics. Authorea Prepr..
Rautiainen, K., Comite, D., Cohen, J., Cardellach, E., Unwin, M., Pierdicca, N., 2021. Freeze–thaw detection over high-latitude regions by means of GNSS-R data. IEEE Trans. Geosci. Remote Sens. 60, 1–13.
re3data.org, 2021. VMF data server; editing status 2021-08-24; re3data.org - Registry of research data repositories. [dataset]. http://dx.doi.org/10.17616/R3RD2H, last accessed: 2023-10-30.
Rideout, W., Coster, A., 2006. Automated GPS processing for global total electron content data. GPS Solut. 10, 219–228.
Rodriguez-Alvarez, N., Bosch-Lluis, X., Camps, A., Vall-Llossera, M., Valencia, E., Marchan-Hernandez, J.F., Ramos-Perez, I., 2009. Soil moisture retrieval using GNSS-R techniques: Experimental results over a bare soil field. IEEE Trans. Geosci. Remote Sens. 47 (11), 3616–3624.
Roesler, C.J., Morton, Y.J., Wang, Y., Nerem, R.S., 2021. Coherent GNSS-reflections characterization over ocean and sea ice based on spire global CubeSat data. IEEE Trans. Geosci. Remote Sens. 60, 1–18.
RTCA (Firm). SC-159, 2006. Minimum Operational Performance Standards for Global Positioning System/wide Area Augmentation System Airborne Equipment. RTCA.
Ruf, C.S., Chew, C., Lang, T., Morris, M.G., Nave, K., Ridley, A., Balasubramaniam, R., 2018. A new paradigm in earth environmental monitoring with the cygnss small satellite constellation. Sci. Rep. 8 (1), 1–13.
Santi, E., Paloscia, S., Pettinato, S., Fontanelli, G., Clarizia, M.P., Comite, D., Dente, L., Guerriero, L., Pierdicca, N., Floury, N., 2020. Remote sensing of forest biomass using GNSS reflectometry. IEEE J. Sel. Top. Appl. Earth Obs. Remote Sens. 13, 2351–2368.
Scherer, D., Schwatke, C., Dettmering, D., Seitz, F., 2022. ICESat-2 based river surface slope and its impact on water level time series from satellite altimetry. Water Resour. Res. e2022WR032842.
Schneider, R., Godiksen, P.N., Villadsen, H., Madsen, H., Bauer-Gottwein, P., 2017. Application of CryoSat-2 altimetry data for river analysis and modelling. Hydrol. Earth Syst. Sci. 21 (2), 751–764.
Sokolovskiy, S.V., 2001. Tracking tropospheric radio occultation signals from low Earth orbit. Radio Sci. 36 (3), 483–498.
Surface Water Ocean Topography (SWOT), 2024. SWOT level 2 water mask pixel cloud data product, version 2.0. http://dx.doi.org/10.5067/SWOT-PIXC-2.0.
UCAR COSMIC Program, 2022. http://dx.doi.org/10.5065/ZD80-KD74, URL http://cosmic-io.cosmic.ucar.edu/cdaac/login/fidrt/level1a/bitArc/.
Unwin, M.J., Pierdicca, N., Cardellach, E., Rautiainen, K., Foti, G., Blunt, P., Guerriero, L., Santi, E., Tossaint, M., 2021. An introduction to the HydroGNSS GNSS reflectometry remote sensing mission. IEEE J. Sel. Top. Appl. Earth Obs. Remote Sens. 14, 6987–6999.
U.S. Geological Survey, 2016. National water information system data available on the world wide web (USGS water data for the nation). accessed [20 July 2024], at URL [http://waterdata.usgs.gov/nwis/].
Wang, Y., Breitsch, B., Morton, Y.T.J., 2020. A state-based method to simultaneously reduce cycle slips and noise in coherent GNSS-R phase measurements from open-loop tracking. IEEE Trans. Geosci. Remote Sens. 59 (10), 8873–8884.
Wang, Y., Morton, Y.J., 2019. Coherent reflections using closed-loop PLL processing of CYGNSS IF data. In: IGARSS 2019-2019 IEEE International Geoscience and Remote Sensing Symposium. IEEE, pp. 8737–8740.
Wang, Y., Morton, Y.J., 2020. Coherent GNSS reflection signal processing for high-precision and high-resolution spaceborne applications. IEEE Trans. Geosci. Remote Sens. 59 (1), 831–842.
Wang, Y., Morton, Y.J., 2021a. Ionospheric total electron content and disturbance observations from space-borne coherent GNSS-R measurements. IEEE Trans. Geosci. Remote Sens. 60, 1–13.
Wang, Y., Morton, Y.J., 2021b. River slope observation from spaceborne GNSS-R carrier phase measurements: a case study. IEEE Geosci. Remote Sens. Lett. 19, 1–5.
Wang, Y., Morton, Y., 2022a. Spaceborne coherent GNSS reflection signal processing over complex terrain. In: Proceedings of the 35th International Technical Meeting of the Satellite Division of the Institute of Navigation. ION GNSS+ 2022, pp. 3671–3676.

Wang, Y., Morton, Y.J., 2022b. Observation of the Mississippi river surface gradients from spire's GNSS-R CubeSats. In: IGARSS 2022-2022 IEEE International Geoscience and Remote Sensing Symposium. IEEE, pp. 4403–4406.

Warnock, A., Ruf, C., 2019. Response to variations in river flowrate by a spaceborne GNSS-R river width estimator. Remote Sens. 11 (20), 2450.

Warnock, A., Ruf, C.S., Knoll, A.L., 2024. Characterization of river width measurement capability by space borne GNSS-reflectometry. Remote Sens. 16 (8), 1446.

Wu, X., Dong, Z., Jin, S., He, Y., Song, Y., Ma, W., Yang, L., 2020. First measurement of soil freeze/thaw cycles in the Tibetan Plateau using CYGNSS GNSS-R data. Remote Sens. 12 (15), 2361.

Yunck, T.P., 1993. Coping with the atmosphere and ionosphere in precise satellite and ground positioning. In: Geophysical Monograph Series, vol. 73, American Geophysical Union, Washington DC, pp. 1–16.

Zakharova, E., Nielsen, K., Kamenev, G., Kouraev, A., 2020. River discharge estimation from radar altimetry: Assessment of satellite performance, river scales and methods. J. Hydrol. 583, 124561.

Zavorotny, V.U., Gleason, S., Voronovich, A.G., 2004. Scattering of GPS signals from the ocean with wind remote sensing application. IEEE Trans. Geosci. Remote Sens. 42 (8), 1665–1675.

Zavorotny, V.U., Larson, K.M., Braun, J.J., Small, E.E., Gutmann, E.D., Bilich, A.L., 2009. A physical model for GPS multipath caused by land reflections: Toward bare soil moisture retrievals. IEEE J. Sel. Top. Appl. Earth Obs. Remote Sens. 3 (1), 100–110.

Zhang, J., Morton, Y.J., 2023. Inland water body surface height retrievals using CYGNSS delay doppler maps. IEEE Trans. Geosci. Remote Sens..

Zhang, J., Morton, Y.J., Wang, Y., Roesler, C.J., 2022. Mapping surface water extents using high-rate coherent spaceborne GNSS-R measurements. IEEE Trans. Geosci. Remote Sens. 60, 1–15.

Zuffada, C., Chew, C., Nghiem, S.V., Shah, R., Podest, E., Bloom, A.A., Koning, A., Small, E., Schimel, D., Reager, J., et al., 2016. Advancing wetlands mapping and monitoring with GNSS reflectometry. In: Living Planet Symposium. Vol. 740, p. 83.